



HAL
open science

The impact of asteroid shapes and topographies on their reflectance spectroscopy

Sandra M. Potin, Sylvain Douté, Benoit Kugler, Florence Forbes

► To cite this version:

Sandra M. Potin, Sylvain Douté, Benoit Kugler, Florence Forbes. The impact of asteroid shapes and topographies on their reflectance spectroscopy. *Icarus*, 2022, 376, pp.114806:1-24. 10.1016/j.icarus.2021.114806 . hal-03500909

HAL Id: hal-03500909

<https://hal.science/hal-03500909>

Submitted on 8 Jan 2024

HAL is a multi-disciplinary open access archive for the deposit and dissemination of scientific research documents, whether they are published or not. The documents may come from teaching and research institutions in France or abroad, or from public or private research centers.

L'archive ouverte pluridisciplinaire **HAL**, est destinée au dépôt et à la diffusion de documents scientifiques de niveau recherche, publiés ou non, émanant des établissements d'enseignement et de recherche français ou étrangers, des laboratoires publics ou privés.



Distributed under a Creative Commons Attribution - NonCommercial 4.0 International License

The impact of asteroid shapes and topographies on their reflectance spectroscopy

S.M. Potin^a, S. Douté^{b,*}, B. Kugler^c, F. Forbes^c

^a*Laboratoire d'Etudes Spatiales et d'Instrumentation en Astrophysique (LESIA), Observatoire de Paris, Université PSL, CNRS, Sorbonne université, Université de Paris, 5 place Jules Janssen, 92195 Meudon, France*

^b*Université Grenoble Alpes, CNRS, Institut de Planétologie et d'Astrophysique de Grenoble (IPAG), Saint-Martin d'Hères, France*

^c*Université Grenoble Alpes, CNRS, Inria, Grenoble INP, Laboratoire Jean Kuntzmann (LJK), Grenoble, France*

Abstract

Here we report the comparison between unresolved reflectance spectroscopy of Solar System small bodies and laboratory measurements on reference surfaces. We measure the bidirectional reflectance spectroscopy of a powder of howardite and a sublimation residue composed of a Ceres analogue. The spectra are then inverted using the Hapke semi-empirical physical model and **the MRTLS parametric model** to be able to simulate the reflectance of the surfaces under any geometrical configuration needed. We note that both models enable an accurate rendering of the reflectance spectroscopy, but the MRTLS model adds less noise on the spectra compared to the Hapke model. Using the parameters resulting from the inversions, we simulate two spherical bodies and the small bodies (1)Ceres and (4)Vesta whose surfaces are homogeneously covered with the Ceres analogue and powder of howardite respectively. We then simulate various scenarios of illumination and spectroscopic observations, i.e. spot-pointing and fly-bys, of these small bodies for phases angles between 6° and 135°. The unresolved reflectance spectroscopy of the simulated bodies is retrieved from the resulting images, and compared to the reflectance spectroscopy of the reference surface measured in the laboratory. Our results show that the photometric

*Corresponding author

Email address: sylvain.doute@univ-grenoble-alpes.fr (S. Douté)

phase curves of the simulated bodies are different from the reference surfaces because of the variations of the local incidence and emergence angles due to the shape and topography of the surface. At low phase angle, the simulated bodies are brighter than the reference surfaces, with lower spectral slope and shallower absorption bands. We observe the maximum differences at wide phase angles with the various simulated observations of (4)Vesta due to its high surface topography. Finally, we highlight the differences in the spectral parameters derived from the unresolved observations at 30° with laboratory measurements acquired under a single geometrical configuration.

Key words: Spectroscopy, Asteroids, surface, Asteroid Ceres, Asteroid Vesta
2021 MSC: 00-01, 99-00

1. Introduction

The Solar System small bodies can be observed from ground-based or Earth orbiting telescopes but only span over a few pixels on the images due to their distance to the observer, their small size, and atmospheric conditions blurring
5 the images (Moreno et al., 2016; Müller et al., 2013; Onaka et al., 2007; Rivkin et al., 2002; Usui et al., 2019). Adaptive optics (AO) systems correct the atmospheric perturbations and increase the spatial resolution of the ground-based telescopes. The sizes and shapes of asteroids can be resolved using AO, though
10 the surface topography is still unresolved (Carry et al., 2010; Marchis et al., 2006; Viikinkoski et al., 2017). The highest spatial resolution on the surface of the small bodies is achieved during in-situ observations by spacecrafts orbiting their targets. In these cases, the small scale topography, boulders and textural variations are observed (Fujiwara et al., 2006; Lauretta et al., 2019; Stern et al., 2019; Watanabe et al., 2019).

15 Moreover, an asteroid presents compositional and textural variations over its surface, and recent close encounters on Near-Earth Asteroids (NEAs) showed multiscales heterogeneities. The spacecraft Hayabusa2 from the Japanese Aerospace eXploration Agency (JAXA) observed compositional heterogeneities on the scale

of the asteroid surface (Kitazato et al., 2019), while its lander, the Mobile Asteroid Surface Scout (MASCOT) observed macroscopic inclusions on the surface of the asteroid (Jaumann et al., 2019). The Origins, Spectral Interpretation, Resource Identification, and Security Regolith Explorer (OSIRIS-REx) spacecraft from the National Aeronautics and Space Administration (NASA) observed dark and bright boulders on the surface of the asteroid Bennu (De-laGiustina et al., 2021). In the case of unresolved spectroscopic observations of asteroids, all these heterogeneities and texture variations are averaged over the whole observed surface.

The dependence of the spectral reflectance on the direction of illumination and observation has been intensively studied. Variations of the albedo with increasing phase angle, i.e. photometric phase curves, were discovered on early observations (Blanco and Catalano, 1979; Gehrels et al., 1970; Lane and Irvine, 1973). The geometry of illumination and observation also impacts the spectral slope and generates the phase reddening, namely the increase of slope, so the increase of the measured reflectance at long wavelengths, with increasing phase angle (Fornasier et al., 2020; Potin et al., 2019; Schröder et al., 2014). The amplitude of the absorption bands that can be detected on the reflectance spectra of asteroids and meteorites is also impacted by the geometry of illumination and observation (Fornasier et al., 2020; Potin et al., 2019).

Reflectance spectroscopy of samples in the laboratory is generally performed under a single geometry, often with a phase angle of 30° with either a nadir illumination or observation (Bishop et al., 1994; Cloutis et al., 2011; De Angelis et al., 2019; Milliken and Mustard, 2005; Pommerol and Schmitt, 2008a; Potin et al., 2020; Takir et al., 2019). Reflectance spectra in the laboratory can only be acquired under a finite number of geometries, depending on the type of instrumental setup and on the studied surface. Moreover, measuring the reflectance spectroscopy of a surface in the laboratory generally required samples with an homogeneous composition and a preliminary preparation of the surface. In order to be statistically relevant, a reflectance spectrometer field of view must take into account a number of facets, randomly oriented, high enough of the sample

50 grains. It thus creates a limitation on the type of sample a spectrometer can
analyse, either fine grained powder, or coarse grains depending on the respec-
tive size of the illumination and observation spots. The study of rock surface is
possible assuming that the sample spans the whole extend of the illumination
spot and is flat enough not to cast shadows on the studied surface, lowering
55 the measured reflectance value. Some setups also necessitate the use of pressed
pellets, or samples must be provided with a fix distribution of grain sizes. All
these parameters restrict the samples availabilities in the laboratory.

We address the following scientific questions. Firstly, to which extent un-
60 resolved topography, roughness, and the overall shape of asteroids are going to
control their reflectance spectra depending on the geometrical acquisition condi-
tions? The study of the effects induced by other unresolved heterogeneities such
as composition and texture will not be the subject of the paper. Then, under
which conditions is it possible to interpret asteroid spectra using reference re-
65 flectance spectroscopy of samples in the laboratory? To answer these questions,
we first propose a methodology (section 2) : we measure the spectral bidirec-
tional reflectance distribution function (BRDF) of asteroidal analogue materials
and we build models of this quantity for any geometry. We examine and dis-
cuss the lab measurements and their modeling (section 3). We then simulate
70 non resolved spectral observations of spherical bodies, Ceres, and Vesta using
the BRDF models and detailed shape models, for a series of acquisition geome-
tries. We describe phase curves in reflectance, spectral slope and band depth
obtained from the simulated observation (section 4). Finally, we discuss the
effects of shape and topography by comparing the reference lab measurements
75 with the simulated results (section 5).

2. Methodology

We propose here to compare for a series of geometries the unresolved spec-
troscopic observation of an asteroidal body to the reflectance spectroscopy of a

flat surface constituted with the same material. To do so, we virtually apply
80 the composition and texture of a surface studied in the laboratory on the shape
model of an asteroidal body. The simulated astronomical target is then placed in
the field of view of a camera and illuminated under a given direction to simulate
sunlight. Each facet of the simulated target will scatter the illuminating light
according to the laboratory BRDF, and integrating the contribution of each illu-
85 minated and observed facet will recreate the unresolved observation of the body.

In this section we describe in details each step of the laboratory measure-
ments, modeling, and integration into the simulation of unresolved observations.

2.1. Presentation of the surfaces

90 Two different samples were used, a sample of howardite and a Ceres ana-
logue. **The sample of howardite consists of a fine powder of the me-
teorite Northwest Africa (NWA) 2060, resulting from the analysis
from Beck et al. (2012). The sample presents a broad distribution of
grain sizes, between 50 and 75 μm . The pyroxene-bearing composi-
95 tion of Vesta, and its relationship to howardite, eucrite and diogenite
(HED) meteorites has been observed first using ground-based tele-
scopic spectrometry and then confirmed during the flight of the Dawn
spacecraft around the small body (De Sanctis et al., 2012; Gaffey,
1997; Longobardo et al., 2014; McSween et al., 2013, 2011; Russell
100 et al., 2012).** The second sample presents a composition similar to the dwarf
planet Ceres, and originating from a sublimation experiment (Schröder et al.,
2021). This sample is mostly composed of magnetite and NH_4 -bearing nontron-
ite, respectively at 44 vol% (63 w%) and 35 vol% (22 w%), with antigorite and
dolomite (De Angelis et al., 2017; Ferrari et al., 2019; Schröder et al., 2021). The
105 residue presents a highly porous texture, and has been studied in bidirectional
reflectance spectroscopy after all sublimation experiments.

2.2. Laboratory bidirectional reflectance spectroscopy

The bidirectional reflectance spectroscopy of the selected surfaces is acquired with the spectro-gonio radiometer SHADOWS (Potin et al., 2018). The spectra
110 are measured from 340 nm to 4200 nm according to the configuration described in table 1.

Range (nm)	Step (nm)	Resolution (nm)
340 - 679	20	4.85 - 4.75
680 - 1499	20	9.71 - 9.38
1500 - 2999	20	19.42 - 18.73
3000 - 4200	20	38.84 - 38.44

Table 1: Spectroscopic configuration of SHADOWS for the bidirectional reflectance spectroscopy of the studied surfaces.

The spectro-gonio radiometer illuminates the sample under a given incidence angle and the reflected light is measured from another fixed angle, defined as the emergence angle. **The phase angle is considered as the angle formed**
115 **by the direction of illumination and observation.** The incidence and emergence angle are calculated with respect to the normal to the surface. In this configuration, a nadir illumination corresponds to an incidence angle of 0°. The measurements can be performed in the principal plane including the normal to the surface and the direction of incidence, or in a plane of any other
120 azimuth angle. Figure 1 shows the geometrical configuration of the spectro-gonio radiometer SHADOWS.

All surfaces are analyzed under the same list of geometrical configurations. The spectra are measured with an emergence angle from -70° to 70° with an angular step of 10°, for an incidence angle going from nadir (0°) to 60° with an
125 angular step of 20° in the principal plane. One series of spectral measurements is also performed out of the principal plane, with an azimuth angle of 30°, an incidence angle of 20° and the emergence angle ranging from -70° to 70° with the same angular step of 10°. It is important to note that the goniometer can-

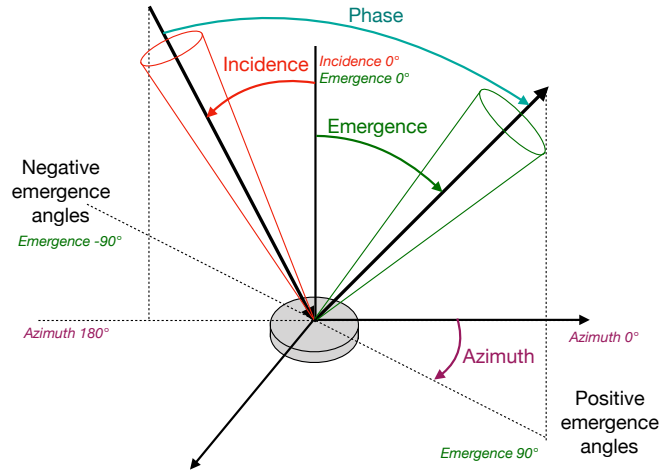


Figure 1: Schematic definition of the geometrical configuration of SHADOWS used in this study. Picture from Potin et al. (2018).

not measure the reflectance of a surface at a phase angle lower than 5° because
 130 of the occultation of the detectors by the incidence mirror. This will have an
 impact on the inversion of the spectra and on the final simulation, which will
 be described in the related sections. The laboratory measurement results in a
 series of 71 different geometrical configurations, for which a single spectrum is
 measured. As the incidence angle is varying along with the emergence angle,
 135 several geometrical configurations result in the same phase angle.

The reflectance factor of the samples is calculated by dividing the measured
 signal for a given sample by the one of a Spectralon and an Infragold targets,
 acquired with a nadir illumination and an observation of 30° .

This measurement method results in a series of 71 spectra for each surface,
 140 each spectrum corresponding to a single geometrical configuration (incidence,
 emergence and azimuth angle). The bidirectional reflectance spectra of each
 composition and texture are presented in appendix.

2.3. Spectral inversion

145 Laboratory measurements on meteorites can only be acquired under a finite
number of geometrical configurations. Inverting photometric models consists in
estimating the best values of their parameters to reproduce the BRDFs sampled
in the laboratory. It is then possible to generate the reflectance spectra that
would have been measured under any geometrical configuration needed for the
150 planetary simulation.

For the analysis of the measured BRDFs we consider two photometric mod-
els: the popular semi-empirical Hapke model based on physical first principles
(Hapke, 1981, 1984, 2008) and a modified version of the Ross-Thick Li-Sparse
model (Lucht and Roujean, 2000; Roujean et al., 1992; Wenner et al.,
155 1995). The latter is a fully parametric model based on a linear combination
of several scattering components, the so-called kernels, that are physically de-
rived from simplified surface and volume scattering scenarii. The kernels pro-
vide the basic BRDF shapes for characterizing the heterogeneous scattering
of soil-vegetation systems and their combination has proved to be accurate in
160 recreating many types of natural surfaces (Jiao et al., 2019, 2016; Mat-
suoka et al., 2016; Schläpfer et al., 2015), including planetary surfaces
(Fernando et al., 2013). The standard Ross-Thick Li-Sparse BRDF model
calculates the reflectance as a weighted sum of three terms:

$$R(\theta, \vartheta, \varphi, \lambda) = f_{iso}(\lambda) + f_{vol}(\lambda) K_{vol}(\theta, \vartheta, \varphi) + f_{geo}(\lambda) K_{geo}(\theta, \vartheta, \varphi) \quad (1)$$

where the terms play the roles of Lambertian (iso), volumetric (vol), and
geometric (geom) components respectively, **with λ the wavelength and the
triplet $(\theta, \vartheta, \varphi)$ representing the incidence, emergence, and azimuth
angles.** Spectral weights f_{iso} , f_{vol} , and f_{geo} **determine the surface re-
flectance properties by controlling the respective contribution of the
three components. Their values do not have a direct physical mean-
ing.** Note that the volumetric kernel contains a simplified treatment of the

opposition effect derived by Bréon et al. (2002) with fixed width and amplitude as this effect is poorly constrained by our measurements:

$$(1 + (1 + \xi/\xi_0)^{-1}) \quad (2)$$

Here ξ is the phase angle, and ξ_0 is a characteristic angle in relation to the ratio of scattering element size and the medium vertical density. We take $\xi_0=1.5^\circ$ that has been suggested as a typical value representing a wide range of surface conditions.

Following Jiao et al. (2019) we add a forward scattering kernel to the standard Ross-Thick Li-Sparse model for a better modeling of the BRDF of our samples:

$$K_{fwd}(\theta, \vartheta, \varphi) = R_0(\theta, \vartheta, \varphi) (1 - \alpha \cdot \cos \xi \cdot \exp(-\cos \xi)) + 0.4076\alpha - 1.1081 \quad (3)$$

The parameter α ensures that the forward scattering kernel is normalized to zero (i.e., $K_{fwd}(\theta, \vartheta, \varphi) = 0$) when the view and sun are both in the nadir direction (i.e., $\theta = 0$ and $\vartheta = 0$). The reflectance R_0 for a semi-infinite, layer of nonabsorbing, large, equant, and translucent particles was derived in an approximate version by Kokhanovsky et al. (2005):

$$R_0(\mu_s, \mu_v, \varphi) = \frac{K_1 + K_2 \cdot (\mu_s + \mu_v) + K_3 \cdot \mu_s \mu_v + P(\xi)}{4 \cdot (\mu_s + \mu_v)} \quad (4)$$

$$P(\xi) = 11.1e^{-0.087 \cdot (180 - \xi)} + 1.1e^{-0.014 \cdot (180 - \xi)} \quad (5)$$

The three constants K are determined by $K_1 = 1.247$, $K_2 = 1.186$, and $K_3 = 5.157$. The parameter ξ is the phase angle (in degrees) and we define $\mu_s = \cos(\theta)$ and $\mu_c = \cos(\vartheta)$. As a result the modified Ross-Thick Li-Sparse (MRTLs) BRDF model calculates the reflectance as a weighted sum of four terms:

$$R(\theta, \vartheta, \varphi, \lambda) = f_{iso}(\lambda) + f_{vol}(\lambda) K_{vol}(\theta, \vartheta, \varphi) + f_{geo}(\lambda) K_{geo}(\theta, \vartheta, \varphi) + f_{fwd}(\lambda) K_{fwd}(\theta, \vartheta, \varphi) \quad (6)$$

For a set of D measurement geometries, each parametrized by a triplet $(\theta, \vartheta, \varphi)$ of incidence, emergence, and azimuth angles, we can model the forward problem as:

$$\begin{aligned}
 R(\theta^d, \vartheta^d, \varphi^d) &= f_{iso} + f_{vol}K_{vol}(\theta^d, \vartheta^d, \varphi^d) + \\
 &f_{geo}K_{geo}(\theta^d, \vartheta^d, \varphi^d) + f_{fwd}K_{fwd}(\theta^d, \vartheta^d, \varphi^d) \quad (7) \\
 &(d = 1 : D)
 \end{aligned}$$

where we omit the wavelength dependency for the sake of simplicity. This set of equations can be reformulated in a matrix form : $\mathbf{R} = \mathbf{K}\mathbf{f}$. The inversion of the MRTLS model can be stated as finding the solution $\mathbf{f}_{sol} = (f_{iso}, f_{vol}, f_{geom}, f_{fwd})$ such that $\|\mathbf{R}_{obs} - \mathbf{K}\mathbf{f}\|^2$ is minimized, \mathbf{R}_{obs} being the vector of reflectance measurements. We use the Maximum Likelihood Estimate to solve the linear regression problem adapted to the kernel formulation of the MRTLS model. In this case the solution of the system of linear equations can be expressed using the pseudo inverse form of matrix \mathbf{K} :

$$\mathbf{f}_{sol} = \mathbf{K}^t (\mathbf{K}\mathbf{K}^t)^{-1} \mathbf{R}_{obs} \quad (8)$$

If the measurements are affected by some uncertainties, expressed by the covariance matrix Σ_{rr} , then these uncertainties can be propagated to the solution using the following equation:

$$\Sigma_{ff} = (\mathbf{K}\mathbf{K}^t)^{-1} \mathbf{K}^t \Sigma_{rr} \mathbf{K} (\mathbf{K}\mathbf{K}^t)^{-1} \quad (9)$$

170 Finally the reflectance values for the measurement geometrical configurations $(\theta, \vartheta, \varphi)$ or any other setting can be computed by inserting the four components of the solution vector \mathbf{f}_{sol} into equation 6. Note that the retrieval of the kernel weights and the modeled reflectance calculation are performed independently for all wavelengths of our measurements.

175

The Hapke model is inverted differently on our measurements because of its highly non-linearity regarding some of its parameters. For that purpose we op-

erate an efficient method based on a learning approach in a Bayesian framework (Kugler et al., In press). The latter offers a natural solution to propagate uncer-
 180 tainties on measures, while the variance of the likelihood assesses the uncertainty induced by the inversion. The high number of geometries and wavelengths to be inverted makes approaches based on Markov Chain Monte-Carlo simulations (Geyer, 1992) unacceptably slow.

The method we propose considers the couple of random variables (\mathbf{X}, \mathbf{R}) ,
 185 where \mathbf{X} is the vector of photometric parameters $(\omega, \bar{\theta}, b, c)$, respectively the scattering albedo, macroscopic roughness, asymmetry parameter and backscattering fraction. The variable \mathbf{X} has an uniform prior distribution on the physical parameters space. The variable \mathbf{R} is the corresponding vector of reflectance values with $\mathbf{R} = F(\mathbf{X}) + \epsilon$ where F is the forward Hapke model and ϵ is a centered
 190 Gaussian noise accounting for measure and model uncertainties.

The main idea is to use a two steps approach. First, we build a parametric surrogate statistical model of (\mathbf{X}, \mathbf{R}) . We choose the family of so-called Gaussian Locally-Linear Mappings (GLLiM) (Deleforge et al., 2015). Such models are expressive enough to approximate highly non-linear, complex, forward mod-
 195 els, while remaining tractable. The learning step is performed by generating a training dictionary composed of samples from (\mathbf{X}, \mathbf{R}) , on which the likelihood is maximized by a standard Expectation-Maximization (EM) algorithm. Regarding the dimensionality of the problem, the number of statistical parameters is proportional to D , the number of measurement geometries, making this
 200 model suitable even for high dimensional observables like ours (71). Moreover, the computational cost of the learning phase is independent of the number of observations to be subsequently analyzed.

In a second step, we use the surrogate model to estimate the posterior probability distribution of the random variable \mathbf{X} given \mathbf{R}_{obs} ($p(\mathbf{X} | \mathbf{R}_{obs})$) inde-
 205 pendently for each observable \mathbf{R}_{obs} , i.e. each wavelength of our goniometric measurements. The inverse of the surrogate GLLiM model has an explicit formulation in the form of a Gaussian mixture. From this posterior density, the mean and variance are straightforward to compute and provide a first order

solution. To refine the solution, the mixture can be further explored with mode
210 search methods and can be exploited in order to perform importance sampling
of the target posterior distribution. Among these alternative solutions (mean,
modes, or importance sampling estimates), the best in terms of the reconstruc-
tion error $\mathbf{X}_{sol} = (\omega, \bar{\theta}, b, c)$ is retained and introduced into the Hapke direct
formulation to compute the reflectance values for the measurement geometrical
215 configurations $(\theta, \vartheta, \varphi)$ or for any other configuration.

2.4. Spectroscopic observation of the target

The measurement of the unresolved reflectance of planetary bodies integrates
their spatial heterogeneities, as well as changes of observation geometries due
to the large-scale structures of the surfaces (slopes, craters, ...) and due to
220 the roughness at small scales. **Our goal is to understand which factors
control the spectrophotometric properties of the objet resulting from
the aggregation of physical signals at different sub-pixel scales. For
that purpose we use a planetary image simulation tool built upon the
physically based renderer Mitsuba¹ that computes light propagation
225 from sources to a scene, and then to a sensor according to ray tracing
and integration schemes.** Several lines of development are considered for
achieving a high degree of realism: high resolution shape models, description
of material distribution, bidirectional reflectance measured in the laboratory as
a function wavelength for analogue materials, mixing of spectral signatures at
230 different scales, 3D radiative transfer of sunlight between the different facets
of the object, and up to the sensor. A synthetic hyperspectral image is gener-
ated according to a given scene, sensor characteristics, and observation ge-
ometry (sub-solar and sub-sensor points, distance between the object and the
observer). The sensor is modeled like a simple pinhole camera defined by its
235 angular field of view, the number of columns, and the number of lines in the
pixel matrix. **The bidirectional reflectance of the surface materials is**

¹Last accessed October 27 2021

expressed either using the Hapke model or the Modified Ross-Thick Li-Sparse (MRTLS) model. The calculation of the spectral radiance at each pixel of the sensor is based on an inverse ray tracing algorithm and MonteCarlo integration scheme. In particular the algorithm addresses the direct illumination on a facet as a function of the local incidence and emergence angles, self-shadowing, occultation, as well as the calculation of the diffuse illumination (i.e. reflections of direct and diffuse irradiance from the neighborhood facets).

In the context of our experiments, we distribute our analogue materials uniformly over the whole shape model of Vesta (Preusker et al., 2014; Russell and Raymond, 2011) and Ceres (Preusker et al., 2016; Roatsch et al., 2016). Each interaction between a ray and a facet involves the calculation of the bidirectional reflectance according to the Hapke or MRTLS model fed by their respective spectro-photometric parameters described in section 3. Note that the computation is conducted for multiple wavelengths in parallel. The final image is expressed for each pixel in the form of a radiance normalized to a unit incoming flux. The shape models of the targets present a spatial resolution of 92m for Vesta and 137m for Ceres, and each pixel thus integrates the spectroscopic contribution of all facets contained in the projection of the pixel onto the surface. The spatial resolution of the resulting images is then fixed by the distance between the target and the observer. The unresolved reflectance spectra resulting from the simulations will not be impacted by a varying resolution as all illuminated and observed facets will contribute to the spectroscopy.

In the context of our experiments, we will consider two scenarii of observation with a series of varying acquisition geometries in both cases: a spot-pointing sequence and a fly-by sequence. In the first case the sensor is always facing the same hemisphere of the object, the sub-observer point is fixed on the surface,

while the sub-solar point moves only in longitude. In the second case the sensor has a straight trajectory in the equatorial plane of the object with a "close encounter" and looks constantly towards the center of the object. Regardless of the scenario, we explore the same series of ten phase angles from 6° to 135° .

3. Results of the bidirectional reflectance measurement and inversion by the models

3.1. Presentation of the spectra and comparison between the two inversed models

To reduce the risk of misinterpretation, it is important that the reflectance spectra resulting from the inversion of the models, and so applied on the surface of our simulated asteroid, are as close as possible to the reference laboratory spectra. We present here the bidirectional reflectance measurement performed on the powder of howardite and on the Ceres sublimation residue, and the spectra resulting from the inversion by the Hapke and MRTLS models. For clarity, we only present the spectra acquired under nadir illumination with an emergence angle of 30° , **and spectra acquired with an illumination angle of 60° and an observation at 70° .**

The reflectance spectrum of the howardite is red-sloped (i.e. increase of reflectance with increasing wavelength) and exhibits absorption features typical of HED meteorites and of their parent body (4)Vesta (De Sanctis et al., 2012). The bands observed around 900 and 2000 nm trace the abundance of pyroxene in the sample, **and their detected positions are linked to the pyroxene mineralogical composition (Burbine et al., 2009, 2018).** Finally, the band detected around 3000 nm indicates the presence of hydroxyl -OH groups linked to hydrated minerals and water molecules (Bishop et al., 1994; Frost et al., 2000).

The Ceres sublimation residue exhibits a broad absorption band centered around 1100 nm related to magnetite in its composition. A strong absorption feature around 2800 nm, and signs of NH₄-bearing organics are detected around

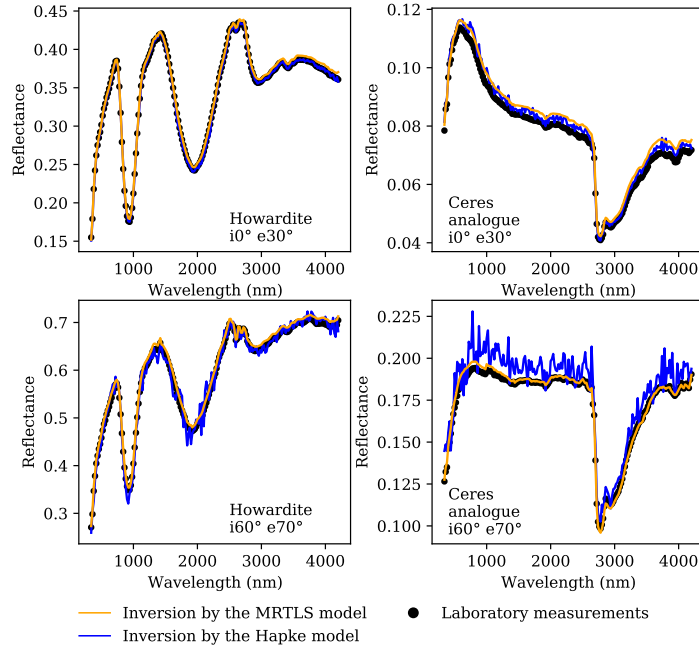


Figure 2: Reflectance spectra of the howardite (left) and Ceres analogue (right) measured in the laboratory (black circles), and resulting from the inversion of the MRTLS model (orange) and the Hapke model (blue). The spectra shown here correspond to the reflectance with a nadir illumination and an emergence angle of 30° (top panels) and with an illumination angle of 60° and an emergence angle of 70° . (bottom panels)

3400 nm (Poch et al. (2020)). The strong blue slope (i.e. decrease of reflectance with increasing wavelength) results from the sublimation experiment giving the sample a highly porous foam-like texture.

300

We can note from figure 2 that the MRTLS and the Hapke models accurately reproduce the spectral features of the initial laboratory spectra. However, reflectance spectra reproduced by the Hapke model exhibit a higher noise compared to the spectra of the MRTLS model or the laboratory spectra, as it can be seen on the Ceres analogue spectrum. **To evaluate the noise added to the spectroscopy by the inversions, the reconstruction error is calculated**

305

here as the absolute value of the difference between the reflectance value resulting from the inversion and the value measured in the laboratory used as reference. Figure 3 presents the reconstruction errors of the Hapke and MRTLS models, considering all geometries at each wavelengths.

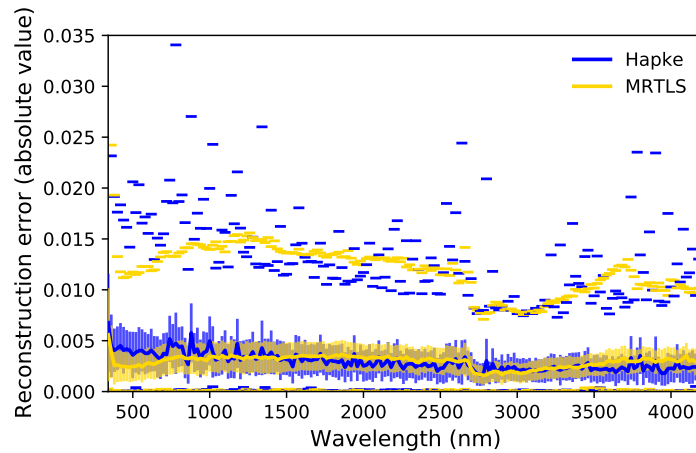


Figure 3: Reconstruction errors of the Hapke (blue) and MRTLS (orange) models, considering all geometries at each wavelength. The solid lines represent the median values, the error bars represent the standard deviation around the median value, the markers are positioned at the minimum and maximum values of the reconstruction error.

Figure 3 shows that the two models result in similar median values of the reconstruction error. However, the standard deviation and maximum values are generally lower on the inversion by the MRTLS model than by the Hapke model. We make the hypothesis that this noise is due to the uncertainties on the Hapke parameters derived during the inversion, impacting the calculated reflectance afterwards.

As the geometry of measurement impacts all spectral parameters, it is important to analyse the ability of the models to accurately recreate the spec-

tra from under any given geometries. As an example, figure 4 presents a polar plot of the reflectance of the surfaces at 560nm, with an incidence angle of 60° . On this representation, the direction of illumination is represented by the red line, and each marker represents a reflectance measurement. The angle from the vertical to the marker corresponds to the emergence angle (here from -70° to 70°), while the length between the marker and the origin corresponds to the reflectance value. In this representation, the BRDF of a perfectly lambertian surface reflecting the light homogeneously in every direction would be represented as a semi-circle.

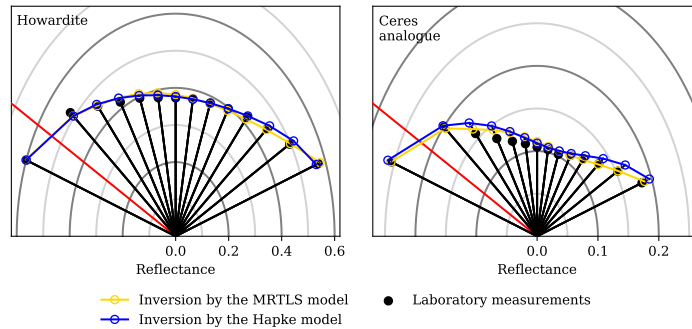


Figure 4: Polar plot of the bidirectional reflectance measured at 560 nm on all surfaces (Left: howardite; Right: Ceres analogue). The reflectance values are taken from the spectra at incidence 60° measured in the laboratory (black), derived from the inversion by the MRTLS model (orange), and derived from the inversion by the Hapke model (blue).

A quantitative analysis of the differences between the laboratory values and those resulting from the inversion is presented further in this section. Both models recreate the bidirectional reflectance behaviour of all surfaces. However, as it can be seen for the howardite and Ceres analogue samples, the Hapke model returns a higher reflectance than the original data in the lobe at high phase angle tracing the forward scattering of the surface. In this region, the MRTLS model returns a closer value of reflectance compared to the Hapke model, and even the accurate value of reflectance in the case of the powdered sample.

Near opposition, where the incidence and emergence follow the same direc-

340 tion creating a phase angle of 0° , the reflectance of a surface increases. This
 opposition surge results from the combination of two phenomena, the Coher-
 ent Backscattering Opposition Effect (CBOE) and Shadow-Hiding backscatter
 Opposition Effect (SHOE) (Hapke, 1986, 2002). Though the laboratory mea-
 345 surements show the beginning of the opposition surge, the spectra from both
 models do not show this increase of reflectance at low phase angle. This results
 from the fact that the reflectance is not measured at the opposition, thus the
 models are not constrained in this area. The spectra resulting from the inver-
 sions consider the reflectance as following the trend constrained by reflectance
 values around the opposition. This results in a method limitation: under a
 350 geometry close to opposition, the reflectance of a simulated body will be under-
 estimated compared to the value of reflectance of the same real body. At phase
 angles wider than 10° , the models accurately reproduce the reflectance of the
 surface, thus the observation will not be biased by the unconstrained opposition
 surge.

355

Along with the value of reflectance, spectroscopic analysis of planetary sur-
 faces is also based on several parameters. The spectral slope is calculated con-
 sidering the reflectance measured at two separated wavelengths as follow:

$$Slope = \frac{R_{\lambda 2} - R_{\lambda 1}}{\lambda 2 - \lambda 1}$$

with R_λ the reflectance measured at the wavelength λ . The band depth is cal-
 culated considering a linear continuum between the two inflexion points around
 the absorption feature:

$$BandDepth = 1 - \frac{R_{center}}{R_{continuum}}$$

with R_{center} the reflectance at the center of the band, **considered as the
 wavelength at which the reflectance is at its minimum value inside
 the absorption feature**, and $R_{continuum}$ the reflectance of the continuum,
 calculated considering a linear continuum and at the same wavelength as the
 360 center of the band.

No apparent shift of the band center is detected on our data with varying illumination and observation geometry. However, the laboratory measurements were acquired with a spectral step of 20nm, so a shift lower than this value would not be detected by the goniometer. No shift of the band center is thus reproduced by the Hapke and MRTLS models, and so will not appear on the BRDFs resulting from the inversions and on the bodies simulations.

To avoid introducing a bias in their estimations, the reflectance and spectral slope must be calculated at wavelengths outside any absorption features. Table 2 presents the wavelengths used for the spectral calculations for the analysis of the howardite and sublimation residue.

	Howardite	Ceres analogue
Reflectance	740 nm	580 nm
Slope	740 - 1380 nm	580 - 2200 nm
Continuum	2720 - 3760 nm	2560 - 3720 nm
Band depth	2960 nm	2760 nm

Table 2: Wavelengths used for the determination of the spectral parameters in the case of the analysis of the howardite and Vesta, and of the sublimation residue and Ceres.

The analysis of the bidirectional behaviour of the reflectance measured on the reference surfaces can be found in appendix. Figure 5 presents the spectral parameters calculated on the laboratory spectra and the set of spectra derived from the Hapke and MRTLS models. All geometrical configurations are plotted on the figure.

The gap between the laboratory spectra and the inversed spectra is considered as the χ^2 of the series, calculated as follow:

$$\chi^2 = \sum \frac{(Spec_{lab}^{(i,e,a)} - Spec_{model}^{(i,e,a)})^2}{\sigma_{lab}^2}$$

with $Spec_{lab}$ and $Spec_{model}$ respectively the spectral parameters measured in

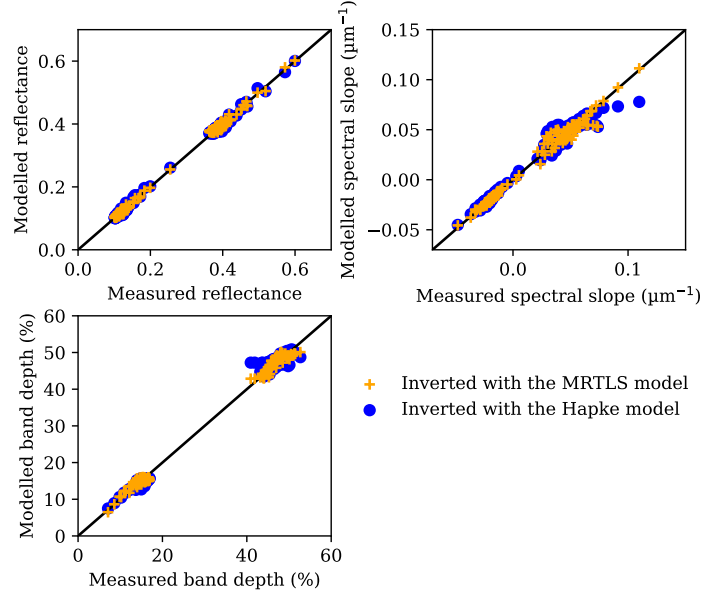


Figure 5: Values of the spectral parameters derived from the spectra resulting from the inversion by the MRTLS model (orange) and the Hapke model (blue), with respect to the measurement values taken as reference (black line).

the lab under the geometry (i.e,a) and the spectral parameters derived from
 380 the Hapke of MRTLS model under the same geometry, and σ_{lab} the error on
 the spectral parameters derived from the laboratory spectra. The model which
 reproduces the most accurately the laboratory data will return the lowest χ^2
 values. The χ^2 values calculated with the series of the spectra derived from the
 Hapke and MRTLS model are presented in table 3.

385

Taking into account all values, the MRTLS model returns a χ^2 value of 2.74
 10^6 while the Hapke model returns a value of 3.35 10^6 . This can come from
 the higher noise shown in the spectra resulting from the inversion by the Hapke
 model. Given the χ^2 value and low noise spectroscopy, we will then use in
 390 priority the MRTLS model in our simulation.

	Howardite		Ceres analogue	
	MRTLS	Hapke	MRTLS	Hapke
Reflectance	2.21 10 ⁶	2.34 10 ⁶	3.53 10 ⁵	6.30 10 ⁵
Slope	3.89 10 ⁴	6.77 10 ⁴	3.22 10 ³	785 10 ³
Band depth	7.18 10 ⁴	5.62 10 ⁴	6.30 10 ⁴	2.43 10 ⁵
Total	2.32 10 ⁶	2.47 10 ⁶	4.19 10 ⁵	8.81 10 ⁵

Table 3: χ^2 values of the spectral inversion by the MRTLS and Hapke models.

4. Results of the simulated scenes

In this section, we present several simulated scenes. The first scenario presents the observation of a simple spherical and homogeneous body, the others present the observation of the targets (1)Ceres and (4)Vesta during spot-
395 pointing protocols and fly-bys. At each time, the target is simulated and observed according to the chosen conditions. The reflectance is averaged over the observed surface in order to obtain an unresolved spectroscopic observation of the body.

400 4.1. Homogeneously covered sphere

As a first test, we select the easiest shape possible for a planetary body. We thus virtually and homogeneously cover a sphere with one of the studied surface and simulate the unresolved spectroscopic observation of this body.

405 As this simulation does not require extensive calculation time, we can consider all combinations of surface composition and reflectance model type (MRTLS or Hapke) and, in each case, we cover the sphere uniformly with the corresponding reflectance. We thus create in total four different simulated spheres.

4.1.1. Unresolved observation at fixed phase angle

410 We first analyse the unresolved reflectance spectra of the simulated spheres at fixed geometry. Figure 6 presents the reflectance spectra of the simulated spheres at phase angle 30° .

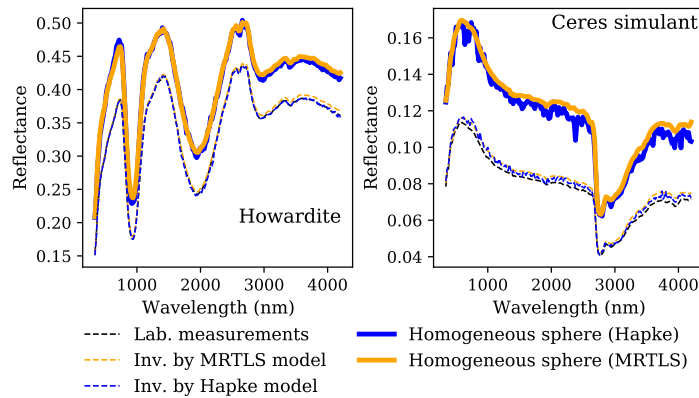


Figure 6: Reflectance spectra at phase angle 30° of the simulated spheres, homogeneously covered with the howardite (left panel) and the Ceres simulant (right panel), and resulting from the inversion by the Hapke (blue) and MRTLS (orange) model. The reflectance spectra of the reference surfaces at incidence 0° and emergence 30° are also plotted in dotted lines (Black: Laboratory measurement, Orange: resulting from the inversion by the MRTLS model, Blue: resulting from the inversion by the Hapke model).

The unresolved simulated spheres present reflectance spectra similar to what
 415 is measured in the laboratory on the reference surfaces. The spectra of the simulated sphere covered with howardite presents the two pyroxene bands around 900 and 2000 nm and the hydration band around 3000nm. The simulated sphere covered with the Ceres simulant also presents the blue slope typical of its reference surface and the strong -OH band around 3000 nm. It has been shown
 420 in previous investigations that a strong slope can hide absorption bands (Potin et al., 2019). But in this case, the effect of shape on the integrated reflectance spectroscopy is not strong enough to alter the spectrum beyond recognition of its composition.

425 However, figure 6 shows that the integrated reflectance spectra of the sim-
ulated sphere are significantly brighter than the reference surface at the same
phase angle. For the howardite, the reference surface presents a reflectance
value of 0.3851 at 740 nm, while the reflectance of the simulated spheres are
of 0.4687 when inverted by the MRTLS model and 0.4737 if inverted using the
430 Hapke model. In this case, the spherical shape of the simulated body increases
the reflectance compared to the reference surface by roughly 0.11. The Ceres
analogue reference surface presents a reflectance value at 580 nm of 0.1138,
while the simulated spheres show a reflectance of 0.1726 when inverted with
the MRTLS model and of 0.1726 when using the Hapke model. In this case,
435 the spherical shape of the simulated body increases the reflectance value by 0.06.

The effect of the shape on the spectral slope and absorption band depth can
hardly been seen on figure 6 and will be further analyzed in the next section
presenting the calculated spectral phase curves. One can expect stronger effects
440 of the shape of the body on its integrated reflectance spectra in the case of a
reference surface showing more drastic variations with the observation geometry
than the surfaces presented here.

4.1.2. Unresolved observation under several phase angles

We now analyse the variations of the spectral parameters with increasing
445 phase angle. The reflectance of the homogeneous spheres is calculated for scenes
of varying illumination and observation geometry, generating phase angles from
1 to 140°. The phase curves, namely the variation of the spectral parameters
with increasing phase angle, are compared to the ones measured in the labora-
tory and derived from the inversion by the Hapke and MRTLS models. Figure
450 7 compares the phase curves of the two simulated objects and their respective
reference surfaces. The laboratory data and spectra derived from the inver-
sion present several points for each value of phase angle, corresponding to the
different incidence angles at which the spectra were acquired and derived.

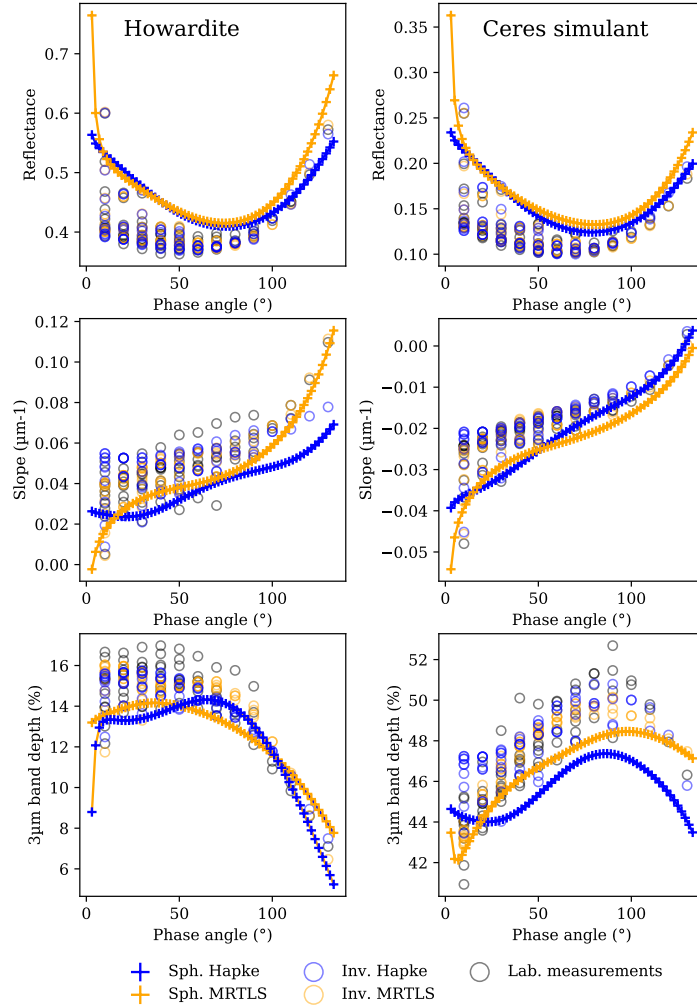


Figure 7: Spectral parameters of the unresolved observation of the simulated spheres homogeneously covered with the howardite and the Ceres analogue. Sph. Hapke: homogeneous sphere covered with the surface derived from the inversion by the Hapke model. Sph. MRTLS: homogeneous sphere covered with the surface derived from the inversion by the MRTLS model. Inv. Hapke: spectral parameters calculated on the spectra resulting from the inversion by the Hapke model. Inv. MRTLS: spectral parameters calculated on the spectra resulting from the inversion by the MRTLS model.

We first notice on figure 7 a difference in the spectral components of the
455 simulated observations with the model used for the inversion. Although the
photometric phase curves (i.e. variations of the reflectance value with increasing
phase angle) of the simulated objects are similar, the variations of the spectral
slope of the sphere simulated by the Hapke model are steeper than the reference
or the sphere simulated with the MRTLS model. The Hapke model returns vari-
460 ations of the band depth with increasing phase angle drastically different from
the reference surface. While the band depths resulting from the inversion by
the MRTLS model follow the convex shape of the reference surface curve, the
Hapke model shows an inflexion of the band depth curve around a phase angle
of 30° , followed by the global decrease of the band depth with increasing phase
465 angle. These variations are due to the noise added to the spectra by the in-
version models. As the MRTLS model has shown to return less noise on the
reflectance spectra and the phase curves, we will apply the parameters derived
from the MRTLS on the next simulated objects.

470 Independently on the inversion model used to simulate the surface, the phase
curves of the simulated spheres are different from the phase curves derived
from the laboratory and inverted spectra. The photometric phase curves of the
simulated objects show higher reflectance than the references spectra on the
whole range of phase angle. The spectral slope of the object simulated with the
475 MRTLS model is globally lower than on the measurements, while the simulation
with the Hapke model returns a spectral slope lower than the reference until
a phase angle of 50° , then higher than the reference. Finally, the simulated
objects show spectral features fainter than their reference surface.

480 The simulated object is homogeneously covered with a single reference sur-
face, so no compositional heterogeneities are involved. Moreover, no terrain
variation has been added to the simulation. This test shows that a spherical
shape is enough to induce noticeable spectral variations between the integrated
reflectance of the target and its surface itself.

485 *4.2. Spot Pointing*

We now add the effect of irregular shape and surface topography to the analysis. Not to add the variations of observed area, we simulate a protocole of spot-pointing around the targets, where the position of the observer is fixed with respect to the surface, and the illumination is movable to change the phase angle. We used the small bodies (1)Ceres and (4)Vesta as simulated targets for this scenario and the next.

To limitate the computation time, we select 10 geometries starting from the lowest phase angle possible for the simulation, so 6° , to 120° in waxing. We also simulated the waning object from 45° to 6° of phase angle. The simulated images of both objects can be found in appendix.

4.2.1. (1)Ceres

We first simulate the spot pointing around Ceres. The altitude of the observer is fixed at 24332 km above the surface. Figure 8 presents the reflectance spectra of the unresolved simulated observations.

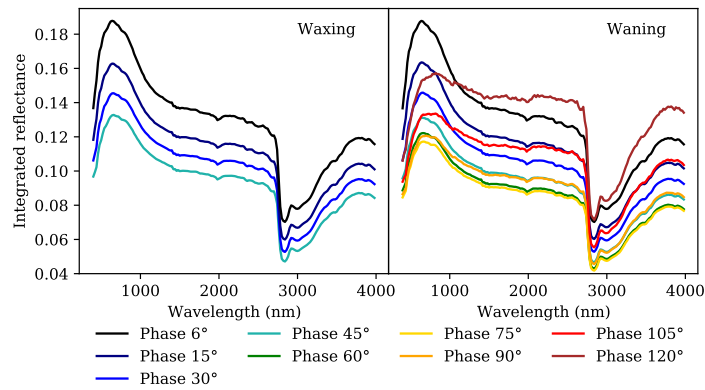


Figure 8: Integrated reflectance spectra of the simulated Ceres observed in spot pointing during waxing (left) and waning (right) phase.

The spectra of the unresolved observations are again similar to the spectroscopy of the reference surface. It is interesting to note here that the spectra derived from the observation of the waxing and waning phases are identicals. In
505 this case, the illumination condition has no effect on the reflectance spectroscopy of the object. However, figure 8 shows that the reflectance of the simulated Ceres decreases for phases angle lower than 75° , then increases back to a value similar to what was observed at low phase angle. Moreover, it can be observed that the spectral slope of the integrated spectra increases, from a strong blue slope at low
510 phase angle to an almost flat spectrum at the widest phase angle simulated here.

We now analyse the variations of the spectral parameters with increasing phase angle. Figure 9 presents the phase curves calculated from the simulated observations.

515

The phase curves of the simulated observations are similar to those of the reference surface, here the sublimation residue of the Ceres analogue. The photometric phase curve shows a concave shape similar to the phase curve of the reference surface, with however a reflectance value higher than what has been
520 measured in the laboratory. The variations of the spectral slope and absorption band depths are also within the range of values of the reference surface. However, the spectral slope of the simulated body tends to be lower than the laboratory measurements. Ceres presents a spherical shape, with small terrain variations compared to its size, so results similar to the first test with the
525 spherical body are expected.

4.2.2. (4)Vesta

Similar to Ceres, we now simulate a spacecraft observing Vesta in spot pointing. The altitude of the observer is fixed at 12166 km above the surface. Figure 10 presents the integrated reflectance spectroscopy derived from
530 the simulated observations.

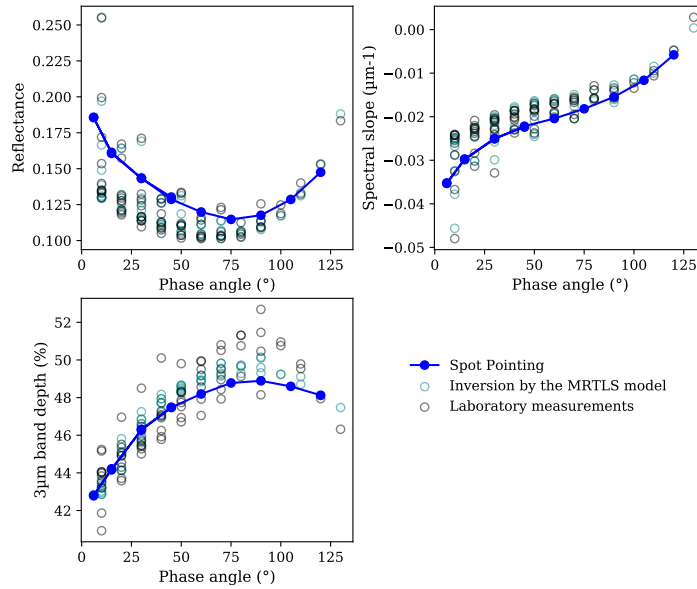


Figure 9: Spectroscopic phase curves of the unresolved observations of Ceres in spot pointing, compared to the spectral parameters derived from the laboratory measurements and inversions by the MRTLS model.

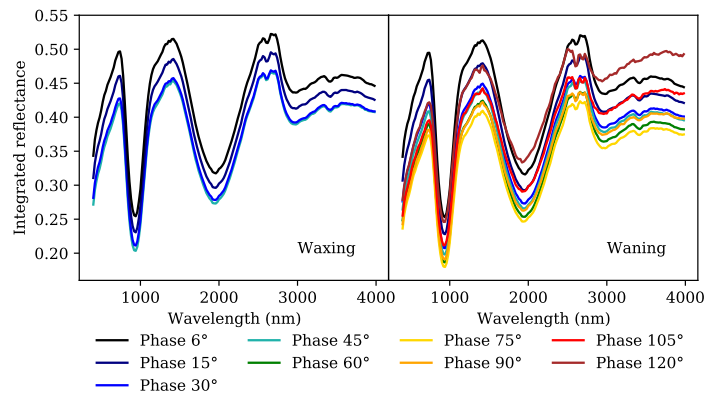


Figure 10: Integrated reflectance spectra of the simulated Vesta observed in spot pointing during waxing (left) and waning (right) phase.

The integrated reflectance spectra of the simulated Vesta show the same pyroxene and hydration absorption features as the reference surface. The differences between the waxing and waning phases of the body are faint and difficult to detect on this figure. However, one can note the decrease of reflectance led by the increasing phase angle, coupled with the increase of the spectral slope.

We now compare the spectral phase curves of Vesta derived from the simulated spot pointing observations. Figure 11 presents the spectral phase curves of Vesta calculated from the simulated observations.

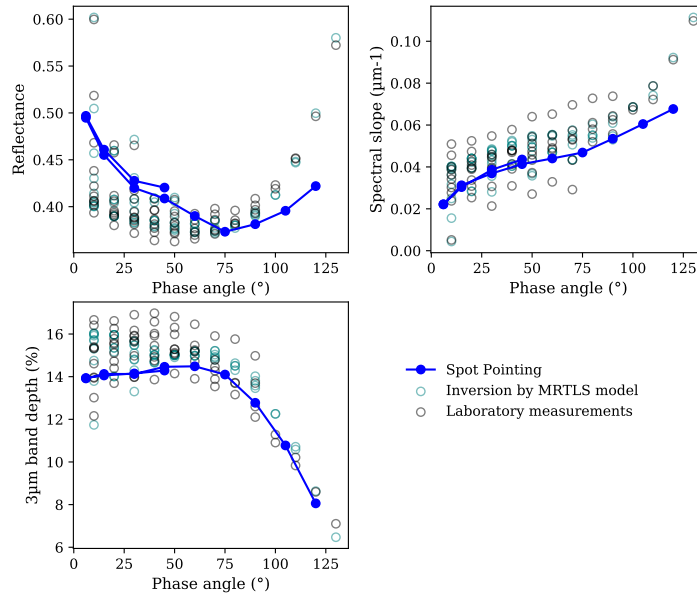


Figure 11: Spectroscopic phase curves of the unresolved observations of Vesta in spot pointing, compared to the spectral parameters derived from the laboratory measurements and inversions by the MRTLS model.

The difference between the waxing and waning phases can only be seen on the photometric phase curve, where the reflectance measured in the waxing phase is slightly greater than in waning phase. At phase angle 45° , the reflectance of

545 the simulated Vesta is of 0.420 in waxing phase for 0.408 in waning phase. The
differences on the spectral slope and absorption band depth are too negligible
in this simulation.

With increasing phase angle, we can observe on figure 11 that the simu-
550 lated observation presents similar phase curves than the reference surface. The
amount of reflectance shows a concave shape with increasing phase angle, with
a minimum met at 75° . The unresolved spectra redden with increasing phase
angle, and the detected band depth decreases. However, when compared to the
reference surface, the simulated Vesta is brighter than what has been measured
555 in the laboratory for phase angles lower than 60° . At wider phase angle, the sim-
ulated Vesta is darker than the reference surface. The two photometric curves
begin to differ at phase angle 90° . The spectral slope derived from the simulated
observations is globally lower than the reference surface. Similar to the photo-
metric phase curve, the divergence from the reference is shown at phase angle
560 90° . Finally, the absorption bands calculated on the simulated observation are
globally shallower than what has been measured in the laboratory, although the
two phase curves do not differ from one another.

The simulation of spot pointing observation implies variations in the illu-
565 mination conditions, such as shadows casted by the topography of the surface.
**However the surface observed on the simulated body is identical in
all observations, as the sub-observer point is fixed on the simulated
surface.**

4.3. Fly-by

570 We now add the variation of the observed surface to the analysis. We thus
simulate the fly-by of the observer near the small bodies Ceres and Vesta. The
small bodies are homogeneously covered with their reference surface, namely
the sublimation residue for Ceres and the howardite for Vesta. In this scenario,
the illumination source and the asteroid are fixed, and the observer is following

575 a straight line, going away from the light source, approaching and then passing
by the small body, pointing toward the center of the target at all time. Obser-
vations are simulated at ten different geometries, ranging from phase angle 6°
to 135° . The simulated images of both objects can be found in appendix.

580 To allow a comparison between the spot-pointing experiment and the fly-by,
the altitude and position of the observer with respect to the surface are set
identical for the phase angle of 30° .

4.3.1. (1)Ceres

We first analyse the simulated fly-by around Ceres. In this scenario, the
585 simulated observer follows a trajectory along the equator of Ceres and is at
an altitude of 12166 km above the surface at his closest approach. Figure 12
presents the resulting reflectance spectra integrated over the whole surface of
Ceres.

590 Similar to the results obtained for Vesta, the increasing phase angle induces
strong variations of the measured reflectance spectroscopy. The reflectance value
in the visible range is measured at 0.201 at phase angle 6° . This value decreases
with increasing phase angle until reaching 0.116 at phase angle 75° . This value
then increases until 0.178 at the widest simulated angle 135° . The spectra of the
595 simulated Ceres present a strongly blue slope at low phase angle, reddening with
increasing angle until a nearly flat spectrum at the widest phase angle simulated.

Figure 13 presents the spectral phase curves derived from the simulated
fly-by around Ceres.

600 It can easily be seen from figure 13 that the spectroscopic phase curves of the
simulated fly-by of Ceres present similar evolution with increasing phase angle
when compared to the reference surface. This behaviour is similar to what
has previously been observed on the homogeneous spheres. We note that the
reflectance value of the simulated Ceres is generally higher than what has been

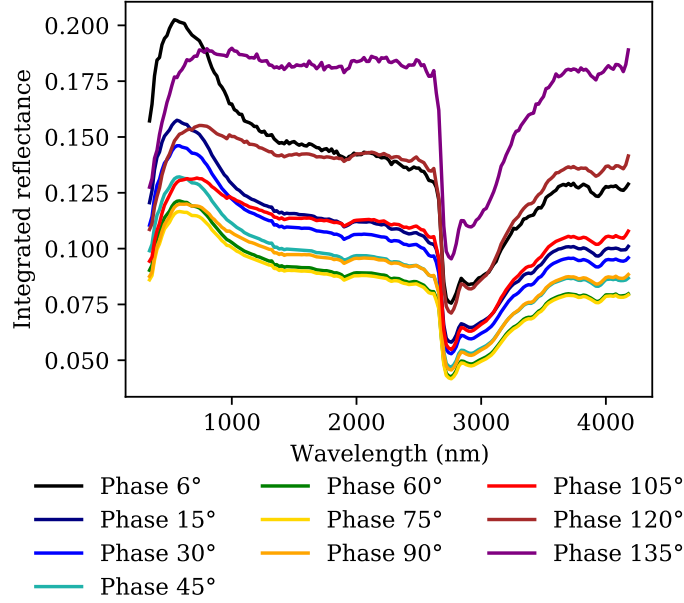


Figure 12: Integrated reflectance spectra of Ceres resulting from the simulated fly-by.

605 measured in the laboratory on the reference surface and the spectral slope is
lower than the reference surface except at phase angle wider than 100°. Finally,
the absorption band depth of the simulated Ceres only becomes lower than most
of the measured values at phase angles wider than 75°.

4.3.2. Equatorial fly-by of (4) Vesta

610 We now simulate the fly-by of the observer around Vesta. The observer tra-
jectory, illumination conditions and observation geometries are similar to the
previous fly-by of Ceres. However, the observer is at an altitude of 6083 km
above the surface at his closest approach. Figure 14 presents the resulting re-
flectance spectra integrated over the whole surface of Vesta.

615

The reflectance spectroscopy of the simulated Vesta presents similar spec-
tral parameters than the reference surface. All spectral signatures, pyroxenes

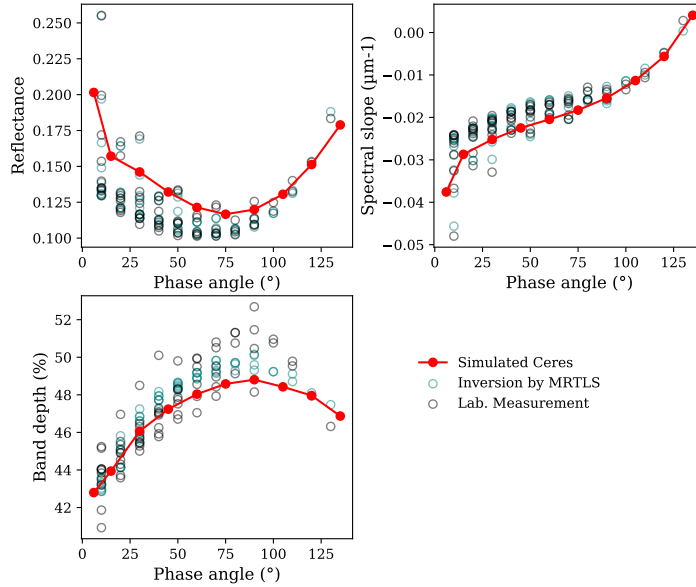


Figure 13: Spectral phase curves resulting from the simulated fly-by around Ceres homogeneously covered with the Ceres analogue. The observations are compared to the spectral parameters derived from the reference surface.

and OH bands, are detected in the spectra throughout the simulation. The reflectance value in the visible range decreases with increasing phase angle, passing from 0.523 to 0.350. Unlike the simulated fly-by of Ceres, no increase of reflectance is observed at wide phase angle. Figure 15 presents the evolution of the spectral parameters with increasing phase angle measured on the simulated equatorial fly-by of Vesta.

We first notice on figure 15 the different behaviours shown by the photometric phase curve of the simulated fly-by. The reflectance decreases within the whole range of phase angles, while the reflectance of the reference surface presents a concave shape, increasing for phase angles wider than 60°. Differences are also present when comparing the spectral slope derived from the fly-by and the reference surface. The phase curve of the simulated object separates from

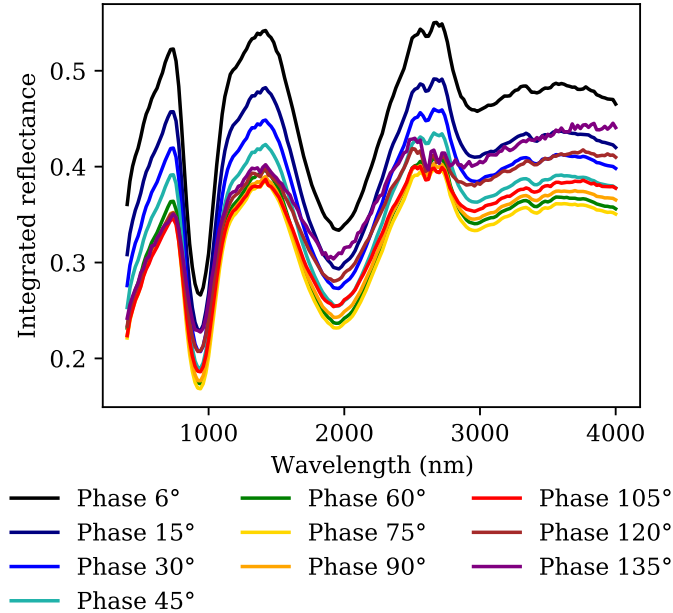


Figure 14: Integrated reflectance spectra of Vesta resulting from the simulated fly-by.

the measurements values around a phase angle of 75° . However, the variations of the band depth with increasing phase angle of the simulated fly-by show the exact variations of the reference surface.

635 For phase angles lower than 45° , the unresolved reflectance of the simulated Vesta is greater than the reference values. The simulated body is then darker than the reference surface at wider phase angle, until reaching a reflectance of 0.35 at phase angle 135° where 0.57 was measured on the reference surface. The spectral slope resulting from the simulation is significantly lower than the reference surface, on the whole angular range. The greater difference is met at the
640 widest simulated phase angle, where a slope of 0.068 is derived from the simulation for 0.110 on the reference surface. Finally, the absorption bands detected on the simulations are shallower than what had been calculated on the refer-

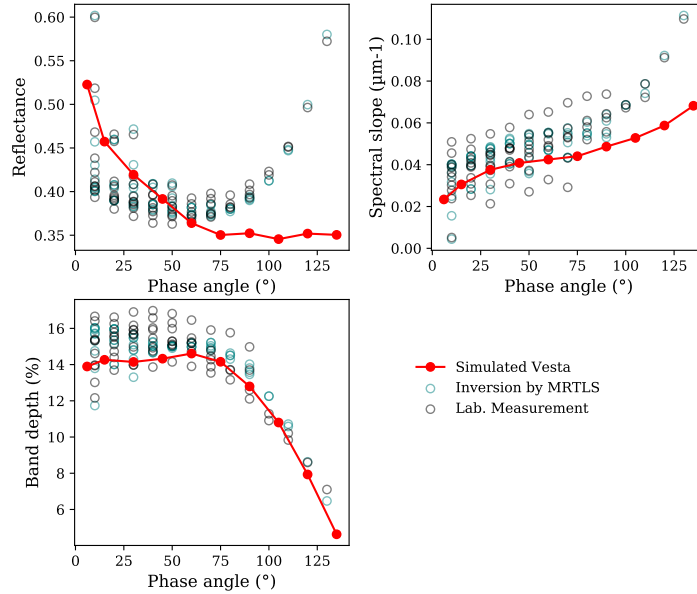


Figure 15: Spectral phase curves resulting from the simulated fly-by around Vesta homogeneously covered with the howardite powder. The observations are compared to the spectral parameters derived from the reference surface.

ence surface, over the whole angular range studied here. At phase angle 30°, the
 645 simulated Vesta presents a 3μm-band depth of 14.15%, while the values derived
 from the reference surface span from 13.3 to 16.9% between the measurements
 and spectral inversion by the MRTLS model.

The surface parameters applied on the simulated Vesta are those resulting
 650 from the inversion by the MRTLS model, based on the laboratory measurements.
 The simulated surface of this Vesta is thus identical to the one measured in the
 laboratory. The body is homogeneously covered with the same composition
 and texture. The only differences between the laboratory measurements and
 simulations are the global shape of the object and the varying observed terrain
 655 on its surface. In this case, the fly-by itself, coupled with a non-spherical shape
 of the body and non-negligeable surface topography are strong enough to induce

drastic differences between the phase curves of the target and its surface in itself.

4.3.3. Polar fly-by of (4)Vesta

In the previous fly-by, both Ceres and Vesta show unvarying shapes along
660 the observations. Ceres is nearly spherical and the fly-by around Vesta was
set along the equatorial ridge of the body, thus observing an oblong shape at
each measurement. To add the variation of shape, we simulate a fly-by around
Vesta, starting from its north pole to the south. During this fly-by, the observed
shape of Vesta goes from a disk at the poles to an oblong shape near the equator.

665

Due to some limitations in the simulation program, the observation of Vesta
with a phase angle of 135° was impossible. The polar fly-by is thus simulated for
phase angles up to 120° . Figure 16 presents the integrated reflectance spectra
of Vesta resulting from this simulation.

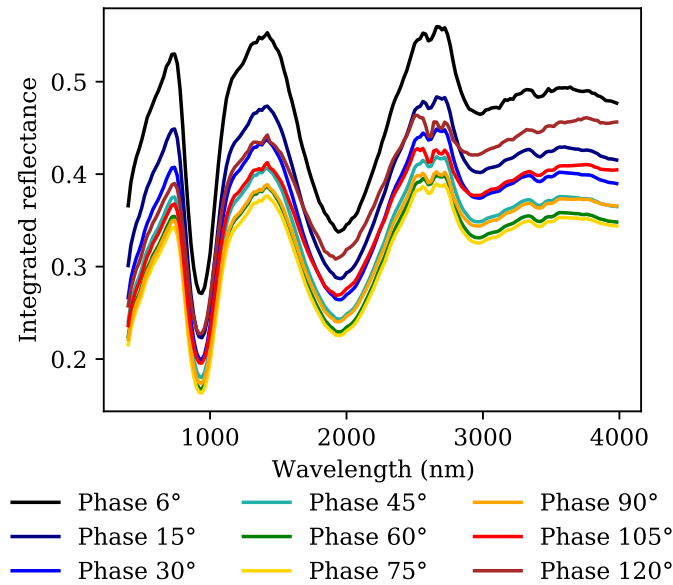


Figure 16: Integrated reflectance spectra of Vesta resulting from the polar fly-by.

670

Similarly to the previous simulations, the unresolved spectra of Vesta calcu-

lated from the polar fly-by show a slightly red slope, as well as the pyroxene and hydration bands. With increasing phase angle, we can note that the reflectance of the simulated body first decreases from 0.530 at phase angle 6° to 0.342 at phase angle 75°. The reflectance then increases until reaching 0.390 at phase angle 120°. Figure 16 also shows that the spectral slope of the simulated Vesta increases with increasing phase angle.

Figure 17 compares the spectral parameters of the reference surface to the phases curves of the simulated Vesta observed during a polar fly-by.

680

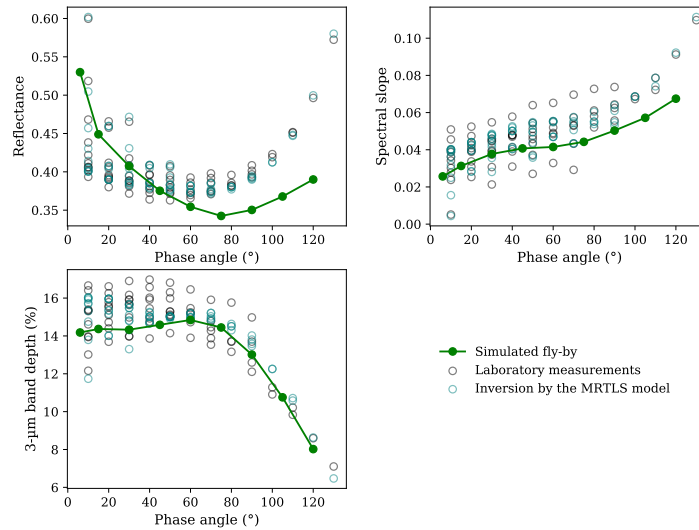


Figure 17: Spectral phase curves resulting from the simulated polar fly-by around Vesta homogeneously covered with the howardite powder. The observations are compared to the spectral parameters derived from the reference surface.

The spectral phase curves derived from the observation show similar behaviours compared to the reference surface. Similar to the results of the previous fly-by along the equator, the observation and reference photometric phase curves differ for phase angles wider than 75°. However, the concave shape shown by

685 the observed photometric phase curve reduces the differences at the widest sim-
ulated phase angle. The unresolved observation of the simulated Vesta presents
a reflectance of 0.39 at phase angle 120° , while the reference surface presents a
reflectance value of 0.57. The evolution of the spectral slope of the simulated
body is similar to the previous fly-by, with, however, lower differences between
690 the phase curves for phase angles wider than 90° . The simulated Vesta returns a
spectral slope of 0.067 at phase angle 120° , for 0.110 measured on the reference
surface. Finally, the evolution with increasing phase angle of the band depth on
the simulated Vesta shows the same convex shape than the reference surface.

695 **Similar to the results obtained with the equatorial fly-by, the phase
curves obtained on the polar fly-by differ from these of the reference
surface.** The simulated body is brighter than the reference surface alone for
phase angles lower than 45° , its spectral slope is lower and absorption bands are
shallower than the reference on the whole angular range.

700

5. Discussion on the effect of shape and topography

We here compare the results from all the simulated scenarii and suggest
reasons for the observed differences in the phase curves. We first analyse the
effect of shape on the reflectance spectroscopy of a planetary body with the
705 comparison between the simulated homogeneous spheres and their reference
surfaces. We then compare the phase curves of the simulated spot-pointings
and fly-bys to assess the effect of topography. Finally, we discuss the potential
bias of comparing unresolved observations and laboratory spectroscopy acquired
under a single geometrical configuration.

710 *5.1. Comparison between the reference surfaces and simulated spheres: The ef- fect of shape*

It has been shown previously on figure 7 that the phase curve of a spherical
body of homogeneous composition differs from the results obtained on its surface

itself, while staying in the range of values of each of its spectral parameters. The
715 global shape of the sphere induces local variations of incidence and emergence
angles on the surface, leading to different geometrical configurations, thus spec-
tral variations. Moving away from the subsolar point, the local incidence angle
changes from nadir to grazing illumination at the limbs, and this effect is similar
for the emergence angle. Both reference surfaces show an increase of reflectance
720 if illuminated and observed at grazing angles (figure 4). The reflectance values
higher than the references measured on the simulated spheres can be due to
the wide area on the spheres showing grazing local angles, thus increasing the
integrated reflectance. The variations due to the spherical shape are responsible
for the higher reflectance value, lower spectral slope and shallower absorption
725 bands of the unresolved simulated body compared to the reference surface.

5.2. Comparison between the different simulated observations: The effect of topography

We now compare for each target the phase curves resulting from the **homo-**
730 **geneous spheres**, spot-pointing and fly-by simulations. Figure 18 compares
the phase curves of the simulated Ceres.

The phase curves resulting from the simulations of Ceres differ from the results obtained with the homogeneous spherical body covered with the Ceres analogue. The simulated sphere is brighter and
735 **shows a bluer slope than than the simulated Ceres over the whole geometrical range studied here. The spherical body also presents a 3- μm absorption band fainter than Ceres for phases angles lower than 100°, the phase curve of the sphere then matches those of the small**
740 **body. We can make the hypothesis that these differences come from the small amount of shadows casted on the surface by the topography.**
The spot pointing and fly-by simulations show almost identical photometric and spectral phases curves. Only the observations under a phase angle of 6° present

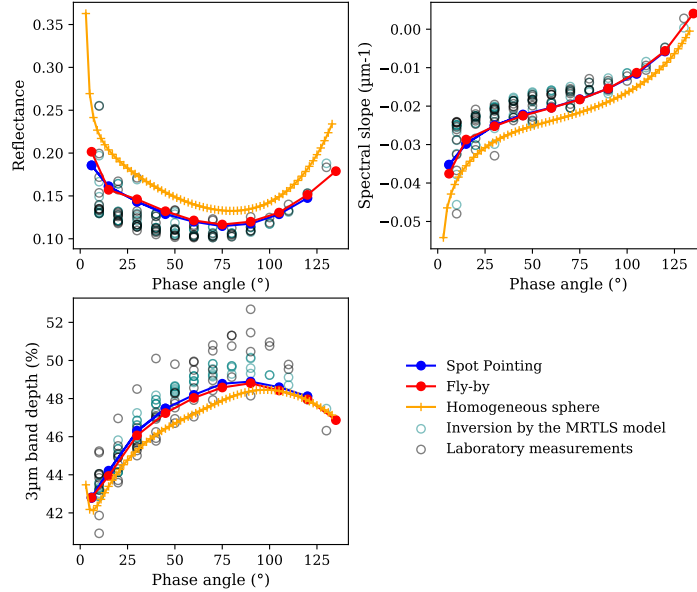


Figure 18: Spectral phase curves resulting from the **simulated spherical body (orange line and markers)**, spot-pointing (blue line and markers) and fly-by (red line and markers) around Ceres, compared to the spectral parameters of the reference surface calculated on the measured spectra (black circles) and resulting from the inversion by the MRTLS model (blue circles).

a noticeable difference, due to the low amount of active pixels for the fly-by.
 745 Identical behaviours with respect to the reference surface are observed for the simulated spot-pointing and fly-by.

The shape of the planetary body and the topography of its surface generates varying directions of illumination and observation on each facet of the shape model. These incidence and emergence angles are then averaged on all
 750 facets included in a single pixel, e.g. the local incidence and emergence angles. Differences in the distribution of these local angles will result in photometric variations, even with a constant phase angle. We now compare the histograms of the local incidence and emergence angles resulting from the simulated spot-

755 pointing and fly-by around Ceres. Figure 19 and 20 presents the distributions of the local incidence and emergence angles respectively.

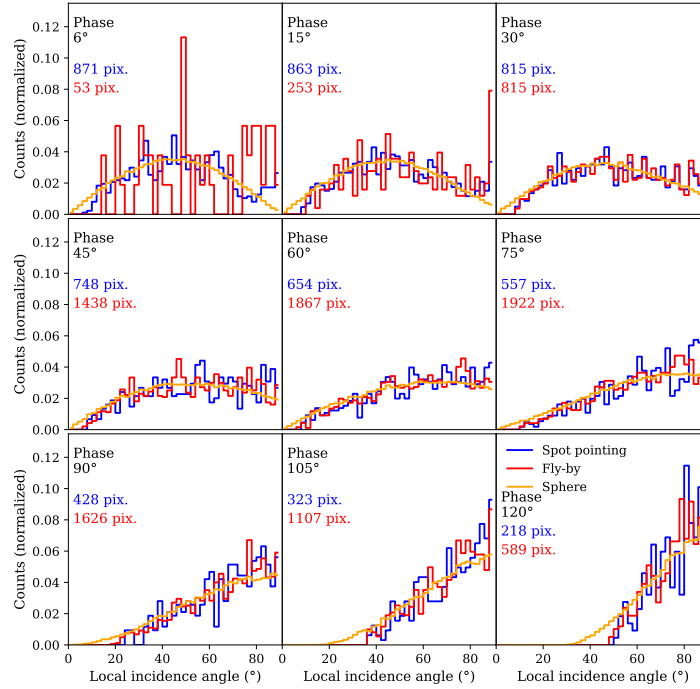


Figure 19: Histograms of the local incidence angles resulting from the spot-pointing (blue) and fly-by (red) around Ceres, **and from the simulation of a spherical body (orange)**. Each panel presents a phase angle. The counts have been normalized to the area under the histogram, so to the total number of pixels illuminated and observed on the images. This number of pixels is indicated on each panel for both the spot-pointing (blue) and fly-by (red).

In the case of Ceres, we observe that the distributions of the local incidence and emergence angles are similar on both simulations, **and follow the distribution of geometries obtained on the spherical body**. The differences of distribution are due to the sampling, i.e. varying with the number of active pixels in each observation, and to the observed area shifting on the simulated body between observations during the fly-by. As the observed topography changes,

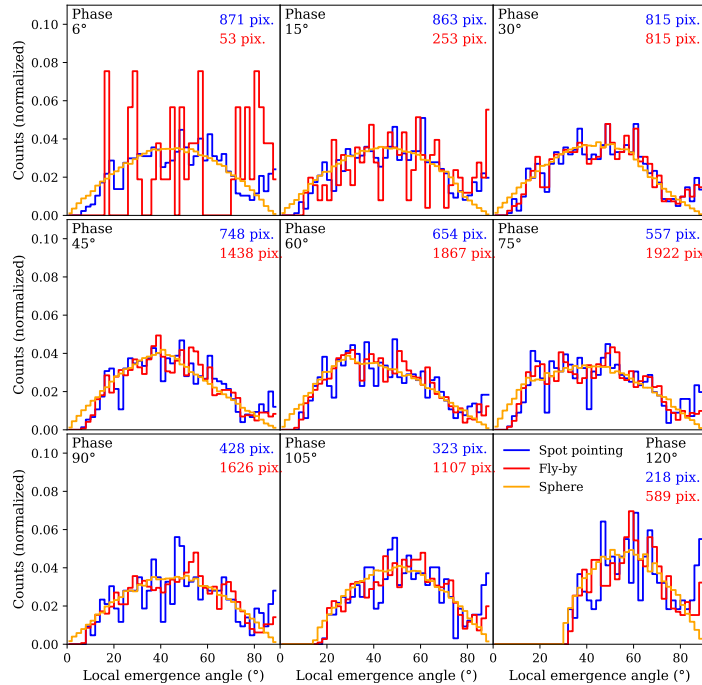


Figure 20: Histograms of the local emergence angles resulting from the spot-pointing (blue) and fly-by (red) around Ceres, **and from the simulation of a spherical body (orange)**. Each panel presents a phase angle. The counts have been normalized to the area under the histogram, so to the total number of pixels illuminated and observed on the images. This number of pixels is indicated on each panel for both the spot-pointing (blue) and fly-by (red).

the distribution of local incidence and emergence angles should change as well.
 765 Because of the spherical shape of Ceres, no variations in shape is observed with increasing phase angle either on the spot-pointing or fly-by simulation. The great similarity between the angular distributions in both simulations **and on the sphere** implies that the variations in topography and observed area have negligible effects in this case. One can suppose that size scale between the diameter of Ceres and its surface topography is too important and smoothen the
 770 geometric variations due to the topography.

We now analyse the differences between the simulated scenarios observing Vesta **and the homogeneous sphere**. We remind that the spot pointing simulation led to variations in the illumination and observation conditions, the equatorial fly-by added a shift of the observed area, and the polar fly-by induced a different observed area and projected shape. Figure 21 compares the phase curves of the simulated Vesta obtained during the spot-pointing, equatorial and polar fly-by.

780

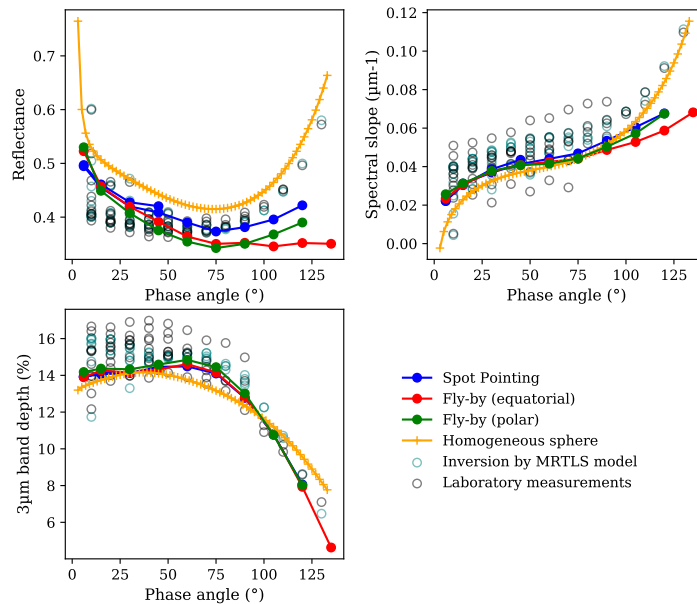


Figure 21: Spectral phase curves resulting from the simulated **homogeneous sphere (orange line and markers)**, spot-pointing (blue line and markers), equatorial fly-by (red line and markers) and polar fly-by (green line and markers) around Vesta, compared to the spectral parameters of the reference surface calculated on the measured spectra (black circles) and resulting from the inversion by the MRTLS model (blue circles).

It is interesting to note that, at low phase angle, the differences between the phase curves of the reference surface and simulated scenarii are similar to the differences observed for a spherical body. The phase curves begin to dif-

fer from phase angles between 60° for the fly-bys or 75° for the spot pointing
785 simulation. One can suggest that at low phase angle, the shadows casted on
the surface by the topography are at the lowest, implying that most observed
spectral variations are due to the shape of the body. At widest phase angle, the
shadows casted on the surface induce a stronger effect of the topography com-
pared to the shape itself, leading to drastic differences between the phase curves.

790

We observe from figure 21 that, unlike the simulations of Ceres, the three
simulated scenarii return different results. The spot pointing simulation returns
the smallest photometric differences with the reference surface. It is interesting
to note that the phase curves resulting from the spot pointing and the polar fly-
795 by simulations present a similar shape, inflexing at 75° , while only the equatorial
fly-by results in a phase curve drastically different from the reference surface.
The spectral slope phase curve resulting from the spot pointing and equatorial
fly-by simulations are almost identical, showing however a slight difference of
0.004 at phase angle 90° . The slope phase curve resulting from the equatorial
800 fly-by differs from the other at phase angles wider than 75° until reaching 0.059
at phase angle 120° , for 0.067 resulting from the spot pointing and polar fly-
by. Finally, the phase curves showing the evolution of the band depth with
increasing phase angle do not show any significant dependency with the sim-
ulation scenario. **The phase curves resulting from all observations of**
805 **the simulated Vesta differ from the phase curves obtained with the**
simulated spherical body. The sphere presents a higher reflectance
than all simulated values over the whole range of phase angles. The
spectral slopes obtained on the sphere are lower than the values re-
sulting from the observation scenarii until 75° of phase angle. The
810 **simulated sphere is then redder than the observation spectra until**
the widest phase angle investigated here. Finally, the amplitude of
the $3\text{-}\mu\text{m}$ band increases until 37° of phase angle, then decreases until
reaching 7.77% at the widest phase angle simulated. In the case of
the observations, the inflexion presented by the phase curves is met

815 **at a phase angle of 60°. The band presented by the spherical body**
is also fainter than its counterpart on the observations, until a phase
angle of 100° where the latest decreases until reaching 4.63% at phase
angle 135° in the case of the equatorial fly-by.

820 We can suppose that this effect is due to the shadows casted on the surface
with increasing phase angle. The general amount of reflectance is lowered by
the increasing shadowed surface, while the spectral slope and band depth are
not impacted by this effect. The photometric phase curves displayed in this
work consider the reflectance in the visible range, while the spectral slope is
825 calculated between the visible and near-infrared range, and the band depth is
calculated in the near-infrared range. We can thus suppose that the effects due
to the shape and topography are stronger at the shorter wavelengths. We thus
analyzed the evolution of the amplitudes of the 1- μm and 2- μm bands detected
on the howardite in the same simulations as presented above. The results are
830 compared to the reference surface and shown on figure 22. The band depths are
calculated using the same formula presented in section 3.1, considering a linear
continuum, between 740nm and 1180nm centered at 940nm for the 1- μm band,
and between 1440nm and 2700nm centered at 1940nm for the 2- μm band.

835 The phase curves both of the 1- μm and 2- μm band for the Vesta and **the**
simulated spherical body experiments, for which howardite uniformly
covers the surface, show similar behaviour to what has been previously ob-
served for the 3- μm band. **The phase curves of the simulated sphere**
present the concave shape similar to the evolution of the 3- μm band,
840 **with amplitudes fainter than what has been measured on the refer-**
ence surface. For the simulations of Vesta, the evolution of the amplitude
of the bands with increasing phase angle follows the reference surface, while how-
ever being shallower than most of the values measured on the howardite. We
can thus conclude from figures 21 and 22 that the effect of shape and topography
845 does not significantly depends on the observed wavelength, at least considering

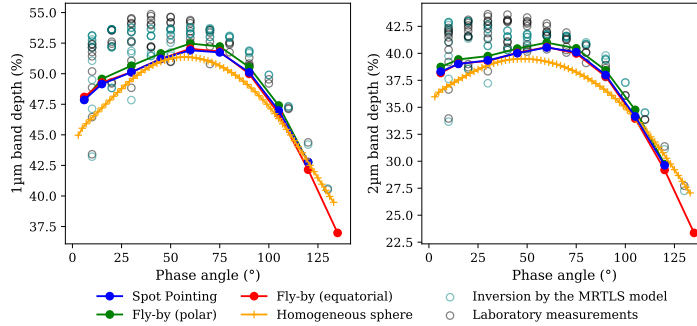


Figure 22: Evolution with increasing phase angle of the amplitude of the absorption bands detected around $1\mu\text{m}$ (left) and $2\mu\text{m}$ (right) on the howardite and the simulated Vesta observations. The values are calculated using the observations from the previous simulations of **the homogeneous sphere (orange line and markers)**, spot-pointing (blue line and markers), equatorial fly-by (red line and markers) and polar fly-by (green line and markers). The values are compared to the band depths of the reference surface calculated on the laboratory measurements (black circles) and spectra resulting from the inversion by the MRTLS model (blue circle).

the spectral range studied here. Textural effects, such as an increase of porosity for example, induce spectral variations depending on the studied wavelengths, as they act on a size scale similar to the wavelength (Hapke, 2008; Schröder et al., 2021). In our case, the size scales of the topography and small body shape are significantly greater than the wavelengths, and so the spectral effects they induce do not depend on the considered wavelength.

Figures 23 and 24 present the distributions of the local incidence and emergence angles on the surface of Vesta observed during the spot-pointing and both fly-by experiments. The correspondent histograms for the sphere experiments are also added.

We observe from figure 23 that the distributions of the local incidence angles are similar on the all scenarii. Moreover, the evolution of the distributions with increasing phase angles is similar to what was observed in the case of

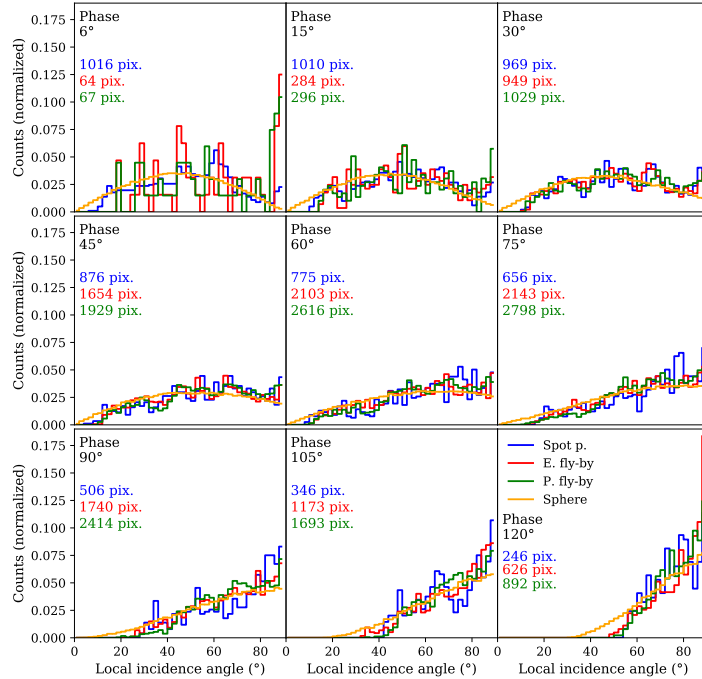


Figure 23: Histograms of the local incidence angles resulting from the spot-pointing (blue), equatorial fly-by (red) and polar fly-by (green) around Vesta, **and from the simulation of a spherical body (orange)**. Each panel presents a phase angle. The counts have been normalized to the area under the histogram, so the total number of pixels illuminated and observed on the images. This number of pixels is indicated on each panel for the spot-pointing (blue), equatorial fly-by (red) and polar fly-by (green).

Ceres (figure 19). At low phase angle, the majority of the facets shows a low incidence angle. The distribution then tilts until the majority of the facets shows a near grazing local incidence angle, at the widest phase angle simulated here. Stronger differences are met when comparing the distributions of the local emergence angles between all simulations. As the spot pointing and the two fly-bys do not observe the same portion of the surface, the distributions of the local emergence, **each departing significantly from the sphere**, trace the various topographies observed, and the changing projected shape of the small body. These variations are seen when comparing the distributions of the local

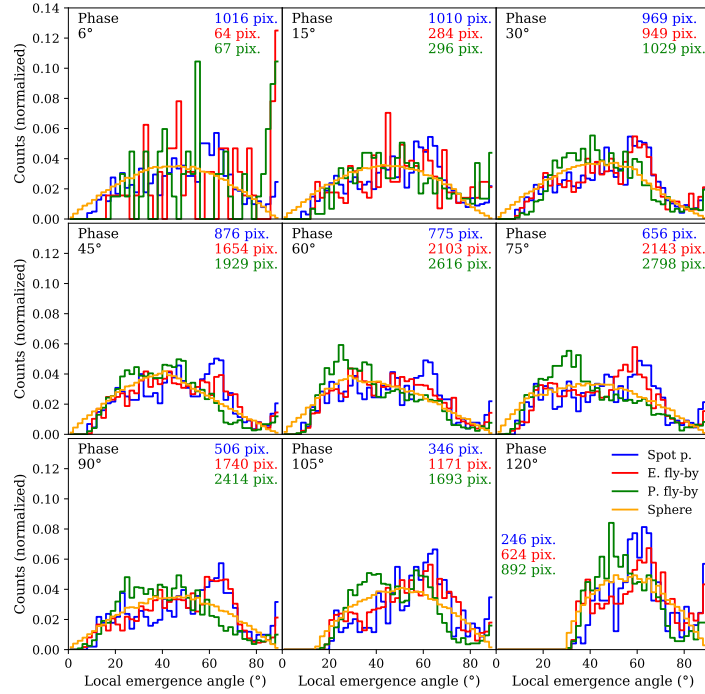


Figure 24: Histograms of the local emergence angles resulting from the spot-pointing (blue), equatorial fly-by (red) and polar fly-by (green) around Vesta, **and from the simulation of a spherical body (orange)**. Each panel presents a phase angle. The counts have been normalized to the area under the histogram, so the total number of pixels illuminated and observed on the images. This number of pixels is indicated on each panel for the spot-pointing (blue), equatorial fly-by (red) and polar fly-by (green).

370 incidence angles, but the differences are fainter than with the local emergence
 angles. We can note on figure 24 that the distribution of local emergence angles
 resulting from the spot pointing simulation show a peak of population between
 25 and 29°, on the complete angular range studied here. This is also shown by
 the equatorial fly-by for phase angles wider than 90°.

875

In the case of Vesta, the non-spherical shape and noticeable topography
 of the surface induce non-negligible variations in the distributions of the local

incidence and emergence angles, depending on the observation scenario. This thus implies the strong differences observed between the phase curves resulting from each simulated observation, and between the small body and its reference surface.

5.3. *The biases in laboratory measurements*

We showed in this study that the phase curves of simulated bodies could differ from the measurements on the reference surfaces acquired under several geometrical configurations. However, bidirectional reflectance spectroscopy can be limited or impossible in the laboratory. The reflectance spectrum is thus generally measured under a single geometry. Table 4 compares the spectral parameters of the spectra obtained for each simulation at phase angle 30° with the spectroscopy of the reference surface acquired in the laboratory with a nadir illumination and an emergence angle of 30° .

The inversion by the MRTLS model induces negligible deviations of the calculated spectral parameters from the reference surface. For the Ceres analogue, the inversion added 2.20% relative to the reflectance value, increases the spectral slope of 4.22% relative and increases the band depth by 1.48% relative. For the howardite, the inversion added 0.39% relative to the reflectance value at 740nm, increases the spectral slope of 6.97% relative and decreases the band depth by 1.09% relative. Our results presented in figure 6 and reminded in table 4 show that the application of the reference surface on a spherical shape induces noticeable variations of the spectral parameters. For the Ceres analogue and howardite respectively, the unresolved observations of the simulated body present higher reflectance value of 48.41% and 21.24% relative, bluer spectral slope of 41.18% and 30.88% relative and absorption bands fainter by 1.22% and 13.31% relative.

We now compare the spectral parameters obtained on the simulated observations. In the case of Ceres homogeneously covered with the analogue, the unresolved spot-pointing observation resulted in an increase of reflectance of

	Analogue	Howardite
Laboratory measurements		
Reflectance	0.1138	0.3851
Slope (μm^{-1})	-0.0213	0.0445
BD (%)	45.28	15.64
Inversion by MRTLS model		
Reflectance	0.1163	0.3866
Slope (μm^{-1})	-0.0204	0.0476
BD (%)	45.95	15.47
Homogeneous sphere		
Reflectance	0.1726	0.4687
Slope (μm^{-1})	-0.0288	0.0329
BD (%)	45.39	13.41
(1)Ceres		(4)Vesta
Spot Pointing		
Reflectance	0.1433	0.4199
Slope (μm^{-1})	-0.0251	0.0369
BD (%)	46.27	14.13
Equatorial fly-by		
Reflectance	0.1461	0.4194
Slope (μm^{-1})	-0.0252	0.0375
BD (%)	46.06	14.15
Polar fly-by		
Reflectance		0.4073
Slope (μm^{-1})		0.0377
BD (%)		14.33

Table 4: Comparison between the spectral parameters derived from the simulated observations and reference surfaces at phase angle 30° . The laboratory measurements and inverted spectra are here presented in the nominal laboratory geometry, with a nadir illumination and emergence angle of 30° . We considered the simulations using the surface resulting from the inversion by the MRTLS model.

23.22% relative, and decrease of the spectral slope of 23.04% relative, while the absorption band depth is not impacted, with an increase of 0.70% relative.

910 The fly-by simulation returns similar deviations of 25.62%, 23.53% and 0.24% respectively for the reflectance, spectral slope and band depth. The phase 30° was used as a reference point to which the simulated object was observe in identical illumination and observation conditions between the various experiments. We noted previously that the phase curves of the simulated Ceres were similar between the spot pointing and fly-by simulation and concluded on the low effect on the reflectance value of the surface topography in the case of Ceres.

915 However, we can note from table 4 that the spectral parameters derived from the simulated Ceres and homogeneous spherical body are different. Considering the homogeneous sphere as reference, the observations of Ceres differ from 16.97 and 15.35% relative for the reflectance value, 12.83 and 12.50% relative for the spectral slope and 1.94 and 1.48% relative for the band depth, for the spot pointing and fly-by respectively. The results suggest that the surface topography of Ceres induces changes in the local incidence and emergence angles acting on the spectral parameters when considered under a single geometrical configuration, but are too shallow compared to the size to induce casted shadows at high phase angle.

920
925

The simulated spot pointing and equatorial fly-by of Vesta resulted in a difference with the reference surface of 8.61% and 8.48% relative for the reflectance value, 22.48% and 21.22% relative for the spectral slope and 8.66% and 8.35% relative for the 3- μm band depth. The polar fly-by returned deviations from the reference surface of 5.35%, 20.80% and 7.37% relative for the reflectance value, spectral slope and 3- μm band depth respectively. In the case of Vesta, the differences of spectral parameters with the spherical body homogeneously covered with the howardite are due to the local angles induced by the non-spherical shape and non-negligible surface topography of Vesta.

930
935

Our results show that when comparing unresolved observations of planetary

body and laboratory spectroscopy acquired under a single geometry, the value
940 of reflectance and the spectral slope are the most impacted parameters. The
unresolved small body returns a higher reflectance value and bluer slope than
its surface alone. These differences are increased if the unresolved body is not
observed under the same phase angle as the laboratory measurement, as shown
by all phase curves simulated in this study. In case of Earth-based observations,
945 asteroids from the Main Belt cannot be observed under phase angles wider
than 30° (Cellino et al., 2014; Rivkin et al., 2019; Usui et al., 2019), comets and
Near-Earth asteroids are observed at phase angles up to 90° (Levasseur-Regourd
et al., 1996; Sanchez et al., 2012), but the Trans-Neptunian Objects can only
be observed near opposition as they are the most distant objects in the Solar
950 System (Rousselot et al., 2005). According to the phase curves resulting from
our simulations, if the target is observed under a phase angle lower than the
laboratory measurement, it will present a greater reflectance value, lower spec-
tral slope and shallower absorption band. To better compare the unresolved
reflectance spectrum of a planetary body with laboratory measurements, it is
955 important to recreate the geometrical configuration of the observation in the
laboratory. This would suppress the effects on the spectral parameters due to
the phase curve of the target, leaving only the effect of shape and surface to-
pography. If the adjustment of the geometrical configuration is not possible for
instrumental reasons or limitations by the sample, one would have to keep in
960 mind the spectral effects due to the different geometries.

We used in this study available reference surfaces consistent with the consid-
ered shape models. One can expect greater differences between the unresolved
observations of the simulated body and its surface itself if the surface presents
965 a stronger spectral dependency with the geometrical configuration. Moreover,
our simulations presented here only consider a simulated body homogeneously
covered with the same surface. Patches of various compositions and textures ap-
plied on the simulated body will increase the difference between the unresolved
observation and laboratory measurement.

970 **Conclusion**

We measured in the laboratory the bidirectional reflectance spectroscopy of a powder of howardite and a sublimation residue of a Ceres analogue. The obtained spectra were inverted using the MRTLS and Hapke models to calculate the reflectance of the surfaces under any geometrical configuration. Comparison
975 between the models show that both accurately result in similar bidirectional behaviour of the surface, though spectra resulting from the inversion by the Hapke model are noisier than the spectra resulting from the inversion by the MRTLS model. We then applied the bidirectional spectroscopic behaviour of the reference surfaces on shape models of spherical bodies and of the small bodies
980 (1)Ceres and (4)Vesta, simulated several unresolved observation scenarii, and compared the obtained phase curves to the laboratory measurements on the reference surfaces.

The reflectance spectra of a spherical body tends to be brighter, bluer and showing fainter absorption features compared to the reference surfaces. These
985 differences from the reference surfaces are due the high area on the spherical surface presenting near grazing local incidence and emergence angles and the strong backscattering behaviour of the reference surfaces used here.

The simulated spot pointing and fly-by of Ceres resulted in phase curves similar to one another, but slightly different from the spherical body covered
990 with the same surface. We concluded that the spherical shape of Ceres coupled with its large size soften the effect of the surface topography, creating however variations of local incidence and emergence angles strong enough to generate a different phase curve from a perfectly spherical body, but not deep enough to create shadows with varying geometrical configuration.

995 We simulated the spot pointing, equatorial fly-by and polar fly-by observations of Vesta. The unresolved reflectance spectra resulted in phase curves strongly different from one another. Moreover, the spectral parameters derived from the observations differ from the laboratory measurements for phase angle wider than 60 or 75°. We showed that the reflectance value is the most impacted

1000 parameter, while the phase curves of spectral slope and amplitude of the ab-
sorption bands approach and sometimes match the laboratory measurements.
These variations are due to these of the local incidence and emergence angles
induced by the shape of the simulated Vesta coupled with its varying surface
topography.

1005 Finally, we presented the differences in spectral parameters between un-
resolved spectroscopic observations of a planetary body with laboratory re-
flectance spectroscopy of the same surface acquired under a single standard
geometry (nadir illumination and emergence angle of 30°). We showed that
unregarding the composition, surface texture and geometry of observation, the
1010 shape and topography of the planetary body will impact its unresolved re-
flectance spectroscopy and generate noticeable differences with the reflectance
spectroscopy of its surface alone.

Acknowledgments

The authors would like to thank Dr. Stefan Schröder for his authorization to
1015 use the BRDF of the sublimation residue of the Ceres analogue. The instrument
SHADOWS was founded by the OSUG@2020 Labex (Grant ANR10 LABX56),
by ‘Europlanet 2020 RI’ within the European Union’s Horizon2020 research and
innovation program (Grant N° 654208) and by the Centre National d’Etudes
Spatiales (CNES).

1020 References

- Beck, P., Pommerol, A., Thomas, N., et al., 2012. Photometry of meteorites.
Icarus 218, 364–377. doi:10.1016/j.icarus.2011.12.005.
- Bishop, J., Pieters, C., and Edwards, J., 1994. Infrared spectroscopic analyses
on the nature of water in montmorillonite. Clays and Clay Minerals 42, 702–
1025 716. doi:10.1346/CCMN.1994.0420606.

- Blanco, C. and Catalano, S., 1979. UVB photometry of Vesta. *Icarus* 40, 359–363.
- Bréon, F., Maignan, F., Leroy, M., and Grant, I., 2002. Analysis of hot spot directional signatures measured from space. *Journal of Geophysical Research* 107, 4282. doi:10.1029/2001JD001094.
- 1030
- Burbine, T., Buchanan, P., Dolkar, T., and Binzel, R., 2009. Pyroxene mineralogies of near-Earth vestoids. *Meteoritics and Planetary Science* 44, 1331–1341. doi:10.1111/j.1945-5100.2009.tb01225.x.
- Burbine, T., Buchanan, P., Klima, R., and Binzel, R., 2018. Can formulas
1035 derived from pyroxenes and/or HEDs be used to determine the mineralogies of V-type asteroids? *Journal of Geophysical Research: Planets* 123, 1791–1803. doi:10.1029/2018JE005561.
- Carry, B., Dumas, C., Kaasalainen, M., et al., 2010. Physical properties of (2) Pallas. *Icarus* 205, 460–472. doi:10.1016/j.icarus.2009.08.007.
- 1040 Cellino, A., Bagnulo, S., Tanga, P., et al., 2014. A successful search for hidden Barbarians in the Watsonia asteroid family. *Monthly Notices of the Royal Astronomical Society : Letters* 439, L75–L79.
- Cloutis, E., Hudon, P., Hiroi, T., et al., 2011. Spectral reflectance properties of carbonaceous chondrites: 2. CM chondrites. *Icarus* 216, 309–346.
- 1045 De Angelis, S., Carli, C., Tosi, F., et al., 2019. NIR reflectance spectroscopy of hydrated and anhydrous sodium carbonates at different temperatures. *Icarus* 317, 388–411. doi:10.1016/j.icarus.2018.08.012.
- De Angelis, S., Ferrari, M., Stefani, S., et al., 2017. IR spectroscopy of ammoniated phyllosilicates and mixtures with relevance for dwarf planet (1) Ceres.
1050 *Proceedings of the European Planetary Science Congress 11, EPSC2017–830.*
- De Sanctis, M., Ammanito, E., Capria, M., et al., 2012. Spectroscopic characterization of mineralogy and its diversity across Vesta. *Science* 336, 697–700. doi:10.1126/science.1219270.

- Deleforge, A., Forbes, F., and Horaud, R., 2015. High-dimensional regression
1055 with gaussian mixtures and partially-latent response variables. *Statistics and
Computing* 25, 893–911. doi:10.1007/s11222-014-9461-5.
- DellaGiustina, D., Kaplan, H., Simon, A., et al., 2021. Exogenic basalt
on asteroid (101955) Bennu. *Nature Astronomy* 5, 31–38. doi:10.1038/
s41550-020-1195-z.
- 1060 Fernando, J., Schmidt, F., Ceamanos, X., et al., 2013. Surface reflectance of
Mars observed by CRISM/MRO: 2. Estimation of surface photometric proper-
ties in Gusev Crater and Meridiani Planum. *Journal of Geophysical Research
(Planets)* 118, 534–559. doi:10.1029/2012JE004194, arXiv:1303.4549.
- Ferrari, M., De Angelis, S., De Sanctis, M., et al., 2019. Reflectance spectroscopy
1065 of ammonium-bearing phyllosilicates. *Icarus* 321, 522–530.
- Fornasier, S., Hasselmann, P., Deshapriya, J., et al., 2020. Phase reddening
on asteroid Bennu from visible and near-infrared spectroscopy. *Astronomy &
Astrophysics* 644, A142. doi:10.1051/0004-6361/202039552.
- Frost, R., Ruan, H., Klopogge, J., and Gates, W., 2000. Dehydration and de-
1070 hydroxylation of nontronites and ferruginous smectite. *Thermochimica Acta*
346, 63–72. doi:10.1016/s0040-6031(99)00366-4.
- Fujiwara, A., Kawaguchi, J., Yeomans, D., et al., 2006. The rubble-pile asteroid
Itokawa as observed by Hayabusa. *Science* 312, 1330–1334. doi:10.1126/
science.1125841.
- 1075 Gaffey, M., 1997. Surface lithologic heterogeneity of asteroid 4 Vesta. *Icarus*
127, 130–157.
- Gehrels, T., Roemer, E., and Zellner, B., 1970. Minor planets and related
objects. IV Asteroid (1566)Icarus. *The Astronomical Journal* 75, 186–195.
- Geyer, C., 1992. Practical Markov Chain Monte Carlo. *Statistical Science* 7,
1080 473–483.

- Hapke, B., 1981. Bidirectional reflectance spectroscopy: 1. Theory. *Journal of Geophysical Research: Solid Earth* 86, 3039–3054. doi:10.1029/JB086iB04p03039.
- Hapke, B., 1984. Bidirectional reflectance spectroscopy: 3. Correction for macroscopic roughness. *Icarus* 59, 41–59. doi:10.1016/0019-1035(84)90054-X. 1085
- Hapke, B., 1986. Bidirectional reflectance spectroscopy: 4. The extinction coefficient and the opposition effect. *Icarus* 67, 264–280. doi:10.1016/0019-1035(86)90108-9.
- Hapke, B., 2002. Bidirectional reflectance spectroscopy: 5. The coherent backscatter opposition effect and anisotropic scattering. *Icarus* 157, 523–534. doi:10.1006/icar.2002.6853. 1090
- Hapke, B., 2008. Bidirectional reflectance spectroscopy: 6. Effects of porosity. *Icarus* 195, 918–926. doi:10.1016/j.icarus.2008.01.003.
- Jaumann, R., Schmitz, N., Ho, T., et al., 2019. Images from the surface of asteroid Ryugu show rocks similar to carbonaceous chondrite meteorites. *Science* 365, 817–820. 1095
- Jiao, Z., Ding, A., Kokhanovsky, A., et al., 2019. Development of a snow kernel to better model the anisotropic reflectance of pure snow in a kernel-driven BRDF model framework. *Remote Sensing of Environment* 221, 198–209. doi:10.1016/j.rse.2018.11.001. 1100
- Jiao, Z., Schaaf, C., Dong, Y., et al., 2016. A method for improving hotspot directional signatures in BRDF models used for MODIS. *Remote Sensing of Environment* 186, 135–151. doi:10.1016/j.rse.2016.08.007.
- Kitazato, K., Milliken, R., Itawa, T., et al., 2019. The surface composition of asteroid 162173 Ryugu from hayabusa2 near-infrared spectroscopy. *Science* 364, 272–275. doi:10.1126/science.aav7432. 1105

- Kokhanovsky, A., Aoki, T., Hachikubo, A., et al., 2005. Reflective properties of natural snow: Approximate asymptotic theory versus in situ measurements. *IEEE Transactions on Geoscience and Remote Sensing* 43, 1529–1535. doi:10.1109/TGRS.2005.848414.
- Kugler, B., Forbes, F., and Douté, S., In press. Fast Bayesian Inversion for high dimensional inverse problems. *Statistics and Computing* .
- Lane, A. and Irvine, W., 1973. Monochromatic phase curves and albedos for the lunar disk. *The Astronomical Journal* 78, 267–277.
- 1115 Lauretta, D., DellaGiustina, D., Bennett, C., et al., 2019. The unexpected surface of asteroid (101955) Bennu. *Nature* 568, 55–60. doi:10.1038/s41586-019-1033-6.
- Levasseur-Regourd, A., Hadamcik, E., and Renard, J., 1996. Evidence for two classes of comets from their polarimetric properties at large phase angles. 1120 *Astronomy & Astrophysics* 313, 327–333.
- Longobardo, A., Palomba, E., F., C., et al., 2014. Photometric behavior of spectral parameters in Vesta dark and bright regions as inferred by the Dawn VIR spectrometer. *Icarus* 240, 20–35. doi:10.1016/j.icarus.2014.02.014.
- Lucht, W. and Roujean, J., 2000. Considerations in the parametric modeling of brdf and albedo from multiangular satellite sensor observations. 1125 *Remote Sensing Reviews* 18, 343–379. URL: <https://doi.org/10.1080/02757250009532395>, doi:10.1080/02757250009532395, arXiv:<https://doi.org/10.1080/02757250009532395>.
- Marchis, F., Kaasalainen, M., Hom, E., et al., 2006. Shape, size and multiplicity of main-belt asteroids. I. Keck Adaptive Optics survey. 1130 *Icarus* 185, 39–63. doi:10.1016/j.icarus.2006.06.001.
- Matsuoka, M., Takagi, M., Akatsuka, S., et al., 2016. Bidirectional reflectance modeling of the geostationary sensor Himawari-8/AHI using a

- kernel-driven BRDF model. *ISPRS Annals of the Photogrammetry, Remote Sensing and Spatial Information Sciences* III-7, 8–13. doi:10.5194/isprsannals-III-7-3-2016.
- 1135
- McSween, H., Binzel, R., De Sanctis, M., et al., 2013. Dawn; the Vesta-HED connection; and the geologic context for eucrites, diogenites and howardites. *Meteoritics and Planetary Science* 48, 2090–2104. doi:10.1111/maps.12108.
- 1140
- McSween, H., Mittlefehldt, D., Beck, A., et al., 2011. HED meteorites and their relationship to the geology of Vesta and the Dawn mission. *Space Science Reviews* 163, 141–174. doi:10.1007/s11214-010-9637-z.
- Milliken, R. and Mustard, J., 2005. Quantifying absolute water content of minerals using near-infrared reflectance spectroscopy. *Journal of Geophysical Research* 110, E12001. doi:10.1029/2005JE002534.
- 1145
- Moreno, F., Snodgrass, C., Hainaut, O., et al., 2016. The dust environment of comet 67P/Churyumov-Gerasimenko from Rosetta OSIRIS and VLT observations in the 4.5 to 2.9 AU heliocentric distance range inbound. *Astronomy & Astrophysics* 587, A155. doi:10.1051/0004-6361/201527564.
- 1150
- Müller, T., Miyata, T., Kiss, C., et al., 2013. Physical properties of asteroid 308635 (2005 YU 55) derived from multi-instrument infrared observations during a very close earth approach. *Astronomy & Astrophysics* 558, A97. doi:10.1051/0004-6361/201321664.
- 1155
- Onaka, T., Kaneda, H., Wada, T., et al., 2007. In-orbit focal adjustment of the AKARI telescope with and without liquid helium cryogen. *Proc. SPIE* 7010, Space Telescopes and Instrumentation 2008: Optical, Infrared, and Millimeter 7010, 70102X. doi:10.1117/12.787725.
- 1160
- Poch, O., Istiqomah, I., Quirico, E., et al., 2020. Ammonium salts are a reservoir of nitrogen on a cometary nucleus and possibly on some asteroids. *Science* 367, eaaw7462.

- Pommerol, A. and Schmitt, B., 2008a. Strength of the H₂O near-infrared absorption bands in hydrated minerals: Effects of particle size and correlation with albedo. *Journal of Geophysical Research E: Planets* 113.
- Pommerol, A. and Schmitt, B., 2008b. Strength of the H₂O near-infrared
1165 absorption bands in hydrated minerals: Effects of measurement geometry. *Journal of Geophysical Research E: Planets* 113, E12008. doi:10.1029/2008JE003197.
- Potin, S., 2018. Bidirectional reflectance spectra (340-4200nm) of powdered howardite and a sublimation residue of a ceres simulant under various geometrical configurations ($i=0^\circ$, 20° , 40° , 60° , $e=-70^\circ$ to 70°).
1170 SSHADE/GhoSST (OSUG Data Center) Sataset/Spectral Data. doi:10.26302/SSHADE/EXPERIMENT_SP_20210814.
- Potin, S., Beck, P., Schmitt, B., and Moynier, F., 2019. Some things special about NEAs: Geometric and environmental effects on the optical signatures
1175 of hydration. *Icarus* 333, 415–428.
- Potin, S., Beck, P., Usui, F., et al., 2020. Style and intensity of hydration among C-complex asteroids: A comparison to desiccated carbonaceous chondrites. *Icarus* 348, 113826.
- Potin, S., Brissaud, O., Beck, P., et al., 2018. SHADOWS: a spectro-gonio
1180 radiometer for bidirectional reflectance studies of dark meteorites and terrestrial analogs: design, calibrations and performances on challenging surfaces. *Applied Optics* 57, 8279–8296.
- Preusker, F., Scholten, F., Matz, K.D., et al., 2016. Dawn at Ceres — Shape Model and Rotational State, in: 47th Annual Lunar and Planetary Science
1185 Conference, p. 1954.
- Preusker, F., Scholten, F., Matz, K.D., et al., 2014. Global Shape of (4) Vesta from Dawn FC Stereo Images, in: *Vesta in the Light of Dawn: First Exploration of a Protoplanet in the Asteroid Belt*, p. 2027.

- 1190 Rivkin, A., Brown, R., Trilling, D., et al., 2002. Near-infrared spectrophotometry of Phobos and Deimos. *Icarus* 156, 64–75. doi:10.1006/icar.2001.6767.
- Rivkin, A., Howell, E., and Emery, J., 2019. Infrared spectroscopy of large, low-albedo asteroids : are Ceres and Themis archetypes or outliers ? *Journal of Geophysical Research : Planets* 124, 1393–1409.
- 1195 Roatsch, T., Kersten, E., Matz, K.D., et al., 2016. High-resolution ceres high altitude mapping orbit atlas derived from dawn framing camera images. *Space Science Reviews* 125, 103–107. doi:10.1007/s11214-011-9836-2.
- Roujean, J.L., Leroy, M., and Deschamps, P.Y., 1992. A bidirectional reflectance model of the earth’s surface for the correction of remote sensing data. *Journal of Geophysical Research: Atmospheres* 97, 20455–20468. doi:https://doi.org/10.1029/92JD01411.
- 1200 Rousselot, P., Petit, J.M., Lvasseur-Rigourd, A., and Muinonen, K., 2005. Polarimetric and photometric phase effects observed on transneptunian object (29981) 1999 TD 10. *Earth, Moon and Planets* 97, 353–364.
- Russell, C. and Raymond, C., 2011. The Dawn mission to Vesta and Ceres. *Space Science Reviews* 163, 3–23. doi:10.1007/s11214-011-9836-2.
- 1205 Russell, C., Raymond, C., Coradini, A., et al., 2012. Dawn at Vesta: Testing the protoplanetary paradigm. *Science* 336, 684–687. doi:10.1126/science.1219381.
- Sanchez, J., Reddy, V., Nathues, A., et al., 2012. Phase reddening on near-earth asteroids : implications for mineralogical analysis, space weathering and taxonomic classification. *Icarus* 220, 36–50.
- 1210 Schläpfer, D., Richter, R., and Feingersh, T., 2015. Operational brdf effects correction for wide-field-of-view optical scanners (brefcor). *IEEE Transactions on Geoscience and Remote Sensing* 53, 1855–1864. doi:10.1109/TGRS.2014.2349946.
- 1215

- Schröder, S., Grynko, Y., Pommerol, A., et al., 2014. Laboratory observations and simulations of phase reddening. *Icarus* 239, 201–216. doi:10.1016/j.icarus.2014.06.010.
- Schröder, S., Poch, O., Ferrari, M., et al., 2021. Dwarf planet (1)Ceres surface bluing due to high porosity resulting from sublimation. *Nature Communications* 12, 274. 1220
- Stern, S., Weaver, H., Spencer, J., et al., 2019. Initial results from the New Horizons exploration of 2014 *mu*₆₉, a small Kuiper Belt object. *Science* 364, eaaw9771. doi:10.1126/science.aaw9771.
- Takir, D., Stockstill-Cahill, K., Hibbits, C., and Nakauchi, Y., 2019. 3- μ m reflectance spectroscopy of carbonaceous chondrites under asteroid-like conditions. *Icarus* 333, 243–251. doi:10.1016/j.icarus.2019.05.012. 1225
- Usui, F., Hasegawa, S., Ootsubo, T., and Onaka, T., 2019. AKARI/IRC near-infrared asteroid spectroscopic survey : AcuA-spec. *Publications of the Astronomical Society of Japan* 71, 1–41. 1230
- Viikinkoski, M., Hanus, J., Kaasalainen, M., et al., 2017. Adaptive optics and lightcurve data of asteroids: Twenty shape models and information content analysis. *Astronomy & Astrophysics* 607, A117. doi:10.1051/0004-6361/201731456.
- Watanabe, S., Hirabayashi, M., Hirata, N., et al., 2019. Hayabusa2 arrives at the carbonaceous asteroid 162173 Ryugu - A spinning top-shaped rubble pile. *Science* 364, 268–272. doi:10.1126/science.aav8032. 1235
- Wenner, W., Li, X., and Strahler, A., 1995. On the derivation of kernels for kernel-driven models of bidirectional reflectance. *Journal of Geophysical Research* 100, 21077–21089. 1240

Appendix A: Bidirectional reflectance spectroscopy of the reference surfaces

Two surfaces are used in reference in this study, and were analyzed with bidirectional reflectance spectroscopy. We present in this appendix the dependencies of the reflectance, spectral slope and amplitude of the absorption bands of the reference surfaces with the geometrical configuration.

A.1. Howardite

We first present the complete set of spectra acquired on the howardite. The spectra are shown in Figure 25.

1250

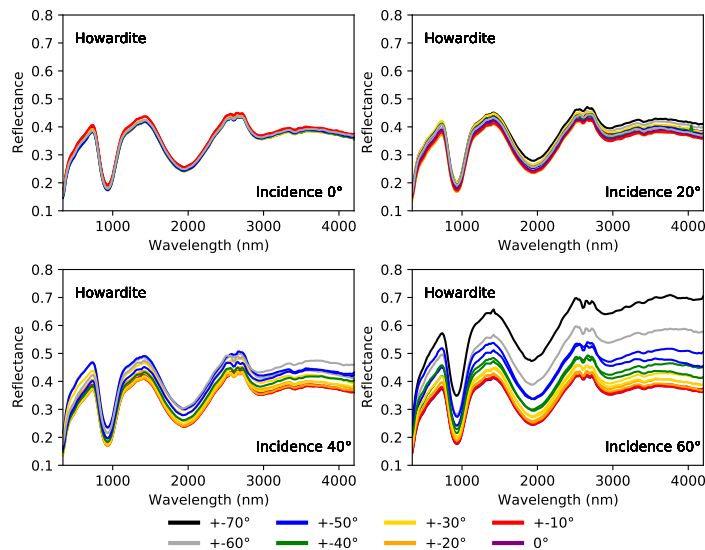


Figure 25: Bidirectional reflectance spectra of the powder of howardite, acquired with an incidence angle of 0° (top left panel), 20° (top right panel), 40° (bottom left panel) and 60° (bottom right panel). The data are available in the GhoSST @ SSHADE database (Potin, 2018).

Figure 25 shows that the bidirectional reflectance spectroscopy of the howardite is increasingly dependent more on the geometrical configuration with increasing

incidence angle, i.e. towards grazing incidence. All spectral parameters, reflectance, spectral slope and absorption bands are now analyzed independently to highlight all effects of the geometrical configurations. Figure 26 presents the variations of the reflectance value at a given wavelength with the geometry.

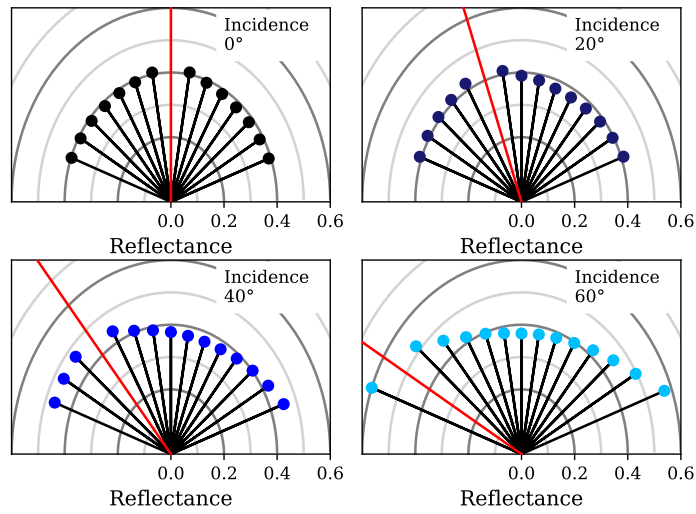


Figure 26: Polar plot of the reflectance measured at 740 nm on the powder of howardite at incidence 0° (top left panel), 20° (top right panel), 40° (bottom left panel) and 60° (bottom right panel). The dots mark the reflectance measurements, and the red line represents the direction of illumination.

The reflectance of the howardite does not show significant variations with the geometrical configuration under nadir illumination (0°). Under grazing incidence (60°), the measured reflectance shows signs of backscattering and forward scattering, inducing an increase of reflectance at low phase angle and around the specular direction respectively. At incidence 60° , the reflectance has been measured at 0.373 at emergence 0° , when 0.599 is measured around the opposition at a phase angle of 10° and 0.496 in the specular direction. The bidirectional reflectance function strongly depends on the surface texture (De Angelis et al., 2019; Pommerol and Schmitt, 2008a; Potin et al., 2019), and in this case, the

sample is a fine powder with a narrow grain size distribution. The shadowing of one particle over another is reduced, which implies a relatively low shadow hiding opposition effect (SHOE, Hapke (1986)) responsible for the increase of reflectance at low phase angle.
1270

Figure 27 presents the variations of the calculated spectral slope with the geometrical configuration, resulting from the reflectance measurement on the howardite.

1275

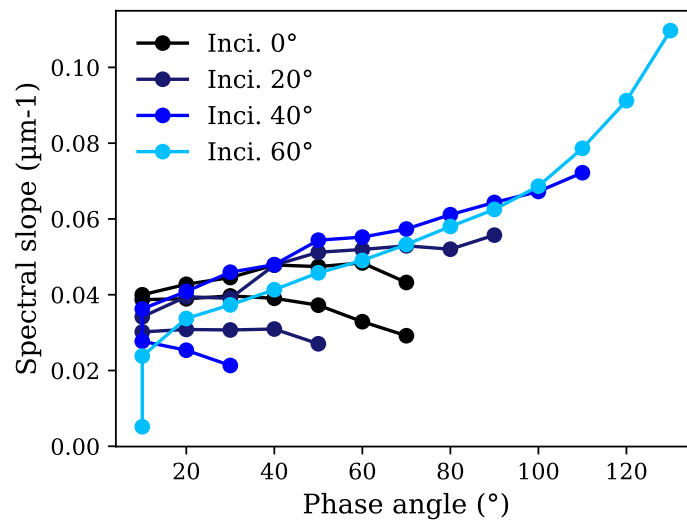


Figure 27: Evolution of the spectral slope with increasing phase angle for the various incidence angles considered here.

Interestingly, the spectral slope derived from the measured spectra does not depend only on the phase angle, but also on the illumination angle. Figure 27 shows that the slope of the spectra acquired with an incidence angle of 0° and 20° generally decreases with increasing phase angle. However, the spectral slope of the spectra acquired at 40° and 60° present the effect of phase reddening, so the increase of spectral slope with increasing phase angle. This effect was
1280

already detected in previous studies (Potin et al., 2019).

Figure 28 presents the variations of the amplitudes of the absorption bands
1285 with the geometrical configuration.

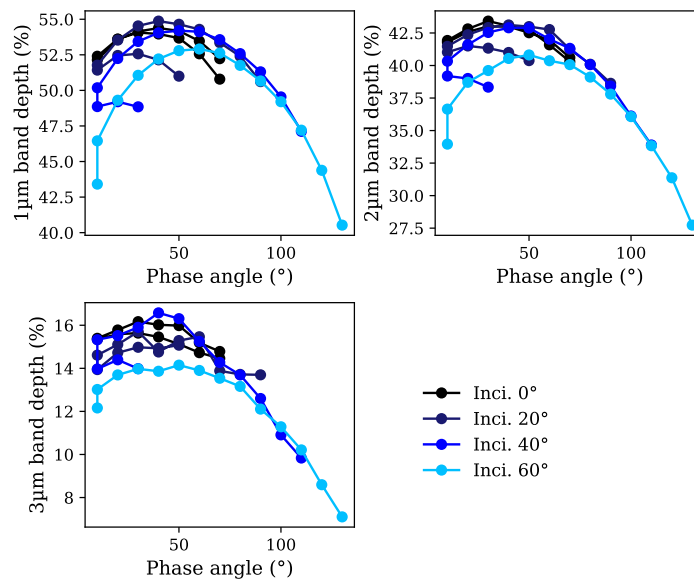


Figure 28: Evolution of the amplitude of the 1- μm (top left panel), 2- μm (top right panel), and 3- μm band (bottom left panel) with increasing phase angle for the various incidence angles considered here.

The three absorption bands detected on the powder of howardite show the
same evolution with increasing phase angle, under all considered incidence an-
gles. All curves show a deepening of the absorption bands until the phase angle
1290 reaches around 40°, then a decrease of amplitude. This effect can be explained
by an increase of the relative number of photons scattered out of the powder be-
fore penetrating the sample and further interacting with the grains (Pommerol
and Schmitt, 2008b). Figure 28 also shows that the amplitude of the absorption
band depends on the illumination angle. For the three bands considered here,

1295 the spectra acquired at incidence 60° presents the shallowest bands, with 46.45,
 36.67 and 13.02% calculated for the 1- μm , 2- μm and 3- μm band respectively at
 low phase angle. In the same configuration, the spectra acquired under a nadir
 illumination returned amplitudes of 52.14, 41.78 and 15.34%.

1300 The reflectance spectroscopy of the powder of howardite shows a clear depen-
 dency of the reflectance, spectral slope and band depth with both the directions
 of illumination and observation.

A.2. Ceres analogue

We now analyze the bidirectional behaviour of the reflectance acquired in
 1305 the laboratory on the sublimation residue of the Ceres analogue. The spectra
 are shown in figure 29.

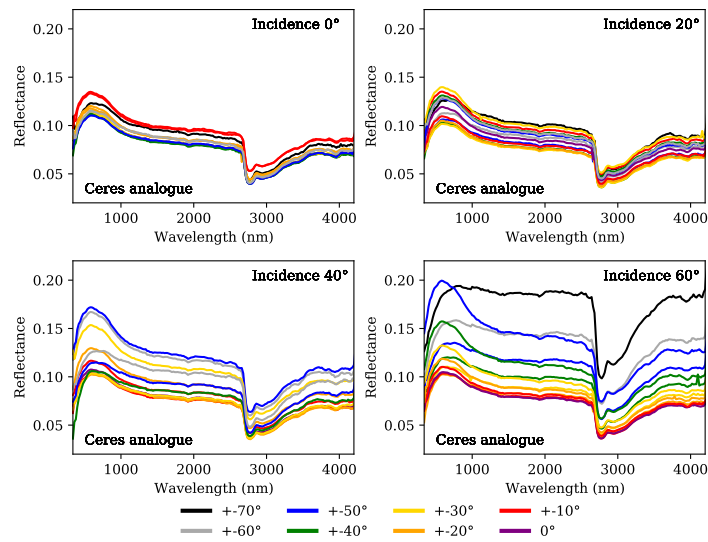


Figure 29: Bidirectional reflectance spectra of the Ceres analogue, acquired with an incidence angle of 0° (top left panel), 20° (top right panel), 40° (bottom left panel) and 60° (bottom right panel). The data are available in the GhosST @ SSHADE database (Potin, 2018).

This sample shows similar dependency with the geometrical configuration to the sample of howardite. The greatest variations between spectra are observed under grazing illumination. The reflectance, spectral slope and absorption bands are now analyzed independently. Figure 30 presents the variations of the reflectance value at a given wavelength with the geometry.

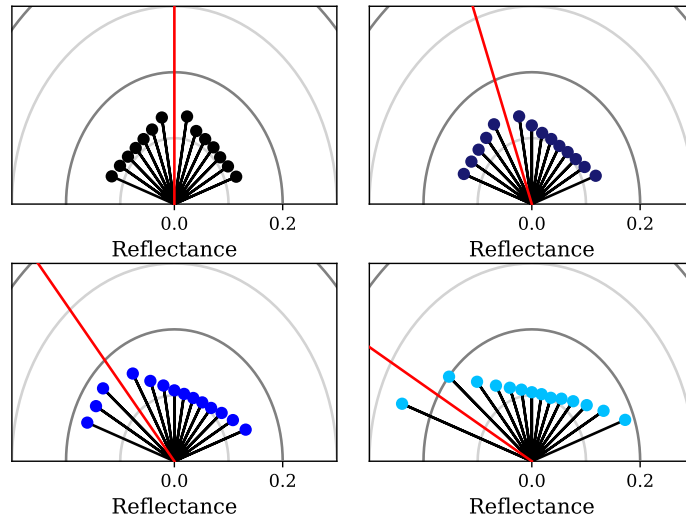


Figure 30: Polar plot of the reflectance measured at 580 nm on the sublimation residue of the Ceres analogue at incidence 0° (top left panel), 20° (top right panel), 40° (bottom left panel) and 60° (bottom right panel). The dots mark the reflectance measurements, and the red line represents the direction of illumination.

The sample of Ceres analogue presents a strong backscattering, i.e. increase of reflectance at low phase angle and for all incidence angles considered here. At a phase angle of 10° , reflectance values of 0.135, 0.140, 0.172 and 0.255 have been measured at incidence 0° , 20° , 40° and 60° respectively, while 0.121, 0.125, 0.140 and 0.183 have been measured at the widest phase angle available for each illumination direction. The high porosity and foam-like texture of the sample increases the amount of shadowing of the grains on their surrounding, and so resulting in an important SHOE effect.

Figure 31 presents the variations of the calculated spectral slope with the geometrical configuration.

1325

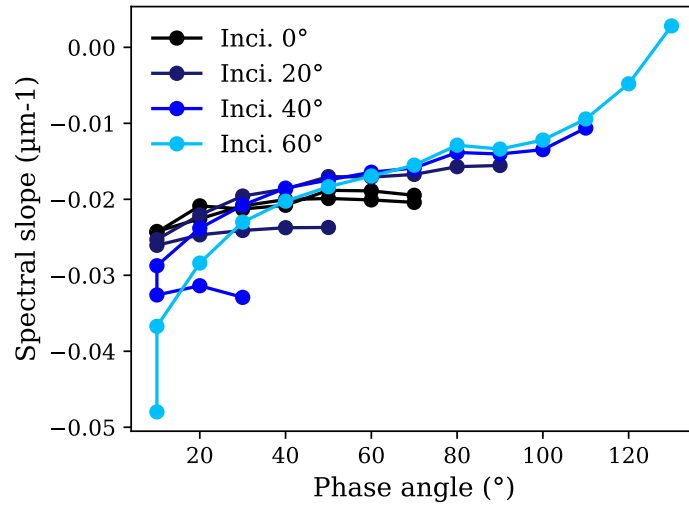


Figure 31: Evolution of the spectral slope with increasing phase angle for the various incidence angles considered here.

The spectral slope derived from the spectra of the Ceres analogue shows the dependency highlighted previously, so on both the directions of illumination and observation. The phase reddening is apparent for spectra acquired at illumination 20°, 40° and 60°.

1330

Figure 32 shows the variation of the amplitude of the absorption band around 3µm with the geometrical configuration.

The 3-µm band detected on this sample shows an deepening for phase angles up to 90°, then a decrease of amplitude. Unlike the results from the howardite, the spectra acquired on the Ceres analogue show deeper absorption bands under

1335

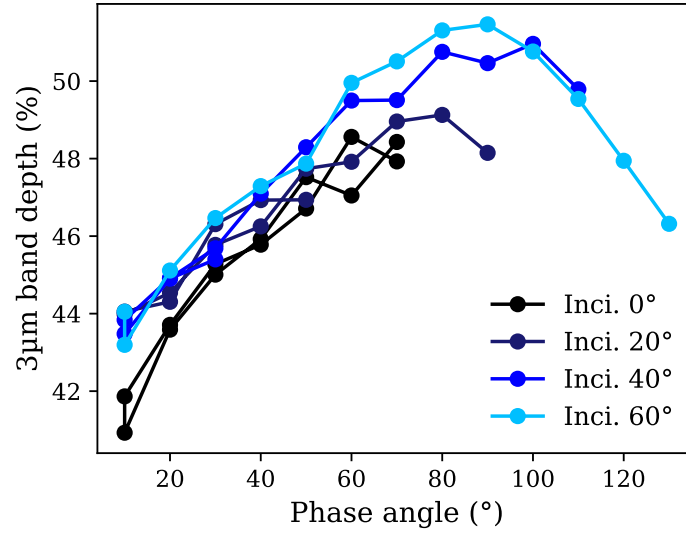


Figure 32: Evolution of the amplitude of the 3- μm band with increasing phase angle for the various incidence angles considered here.

grazing illumination than under nadir. At phase angle 10° , 41.8% has been measured under nadir illumination, for 44.0% under illumination 60° . One can suppose that this effect is due to the foam-like texture of the surface, allowing the photons to penetrate deeper in the sample and interacting with the grains under grazing geometries.

Appendix B: Images of the simulated observations

We present here the various images resulting from the spot-pointing and fly-bys of the simulated Ceres and Vesta, showing the radiance of the bodies at 400nm.

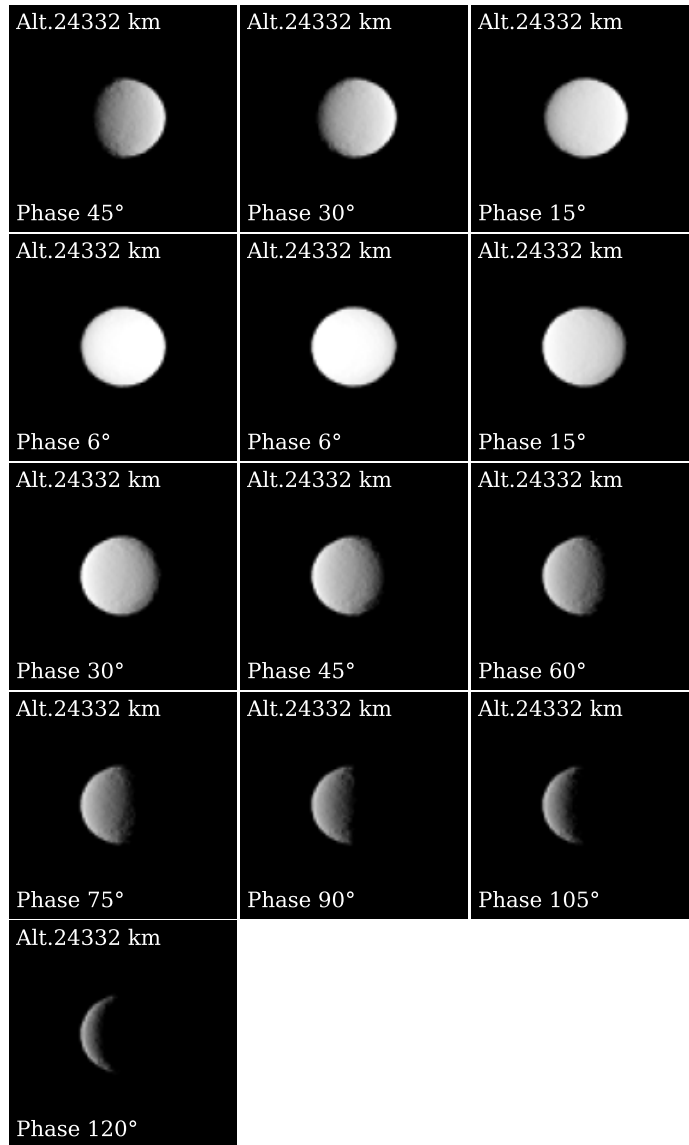


Figure 33: Simulated observations of Ceres resulting from the spot-pointing.

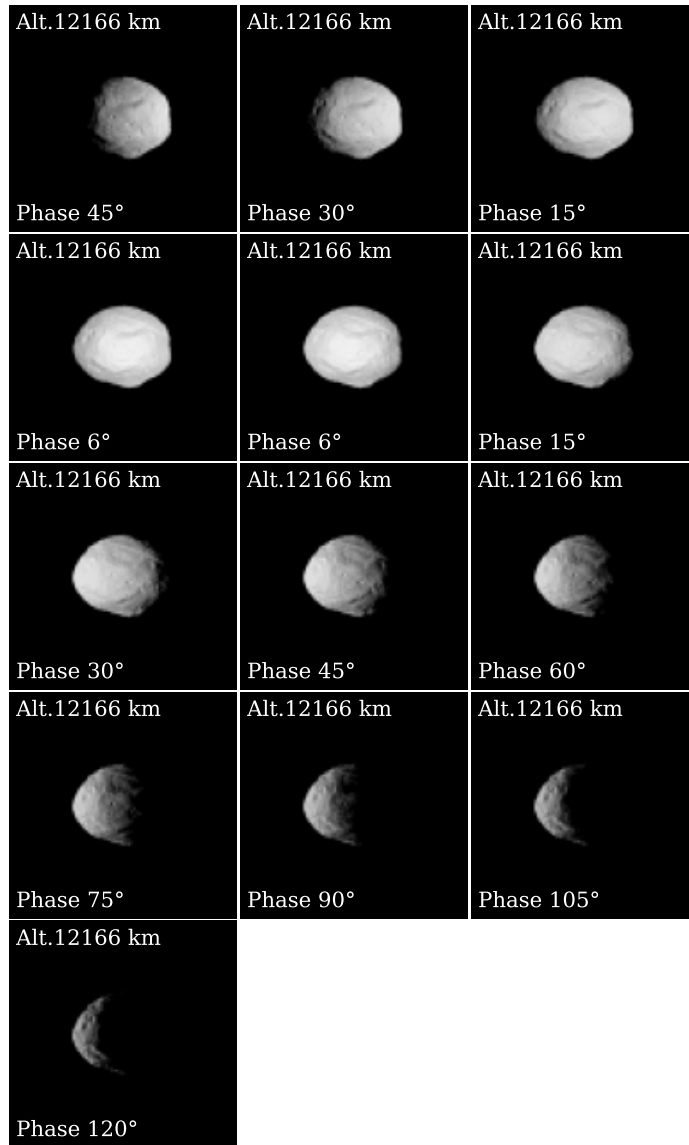


Figure 34: Simulated observations of Vesta resulting from the spot-pointing.

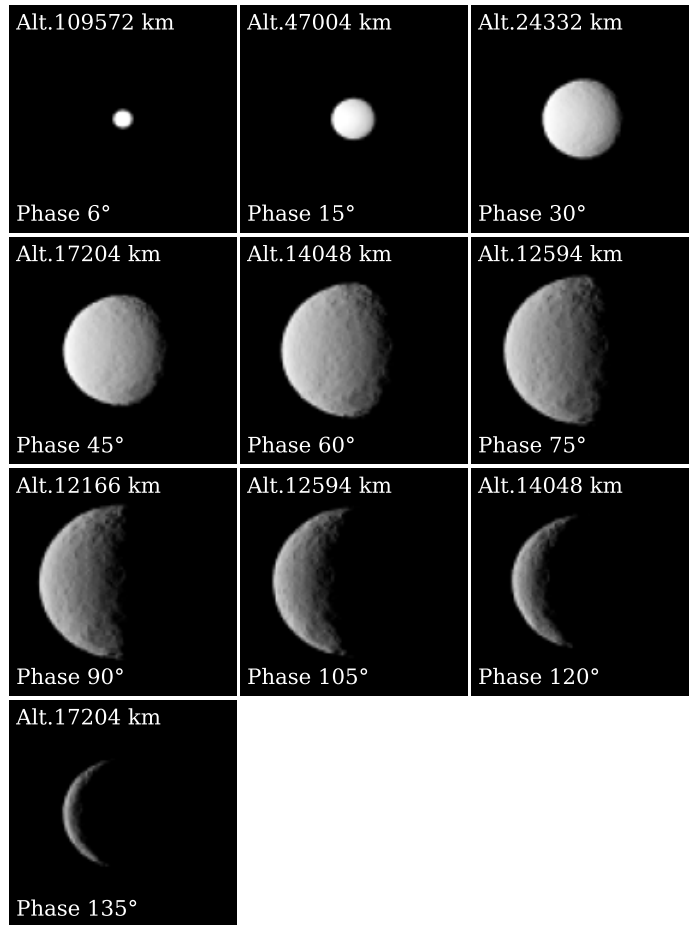


Figure 35: Simulated observations of Ceres resulting from the equatorial fly-by.

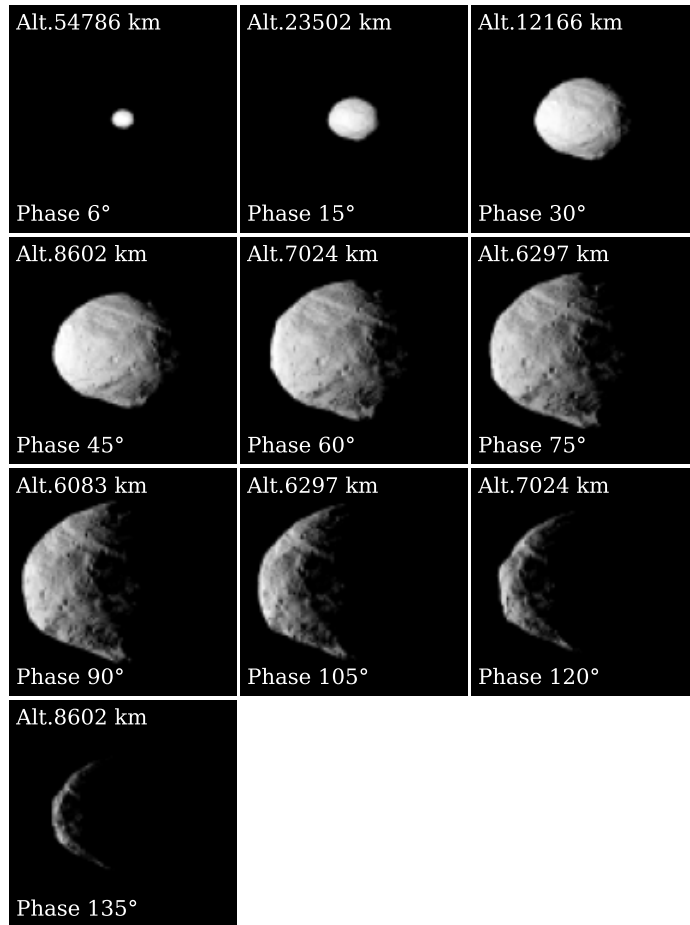


Figure 36: Simulated observations of Vesta resulting from the equatorial fly-by.

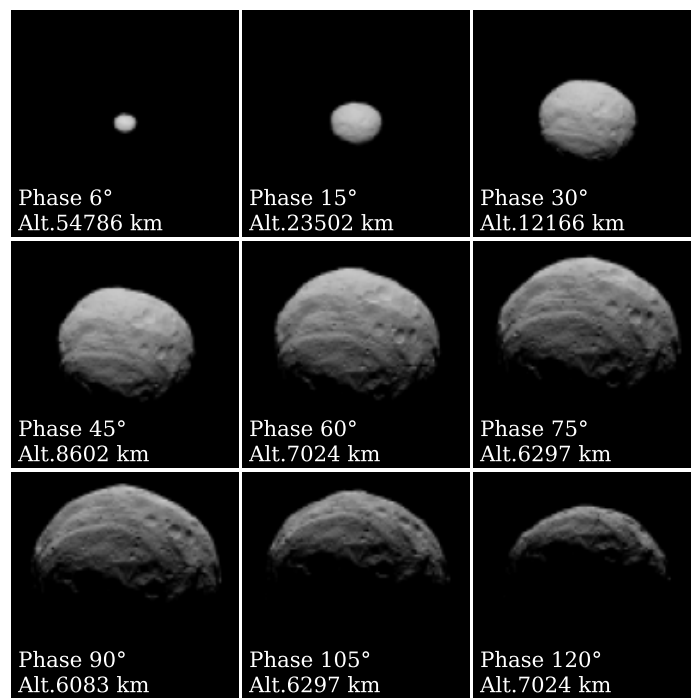


Figure 37: Simulated observations of Vesta resulting from the polar fly-by.